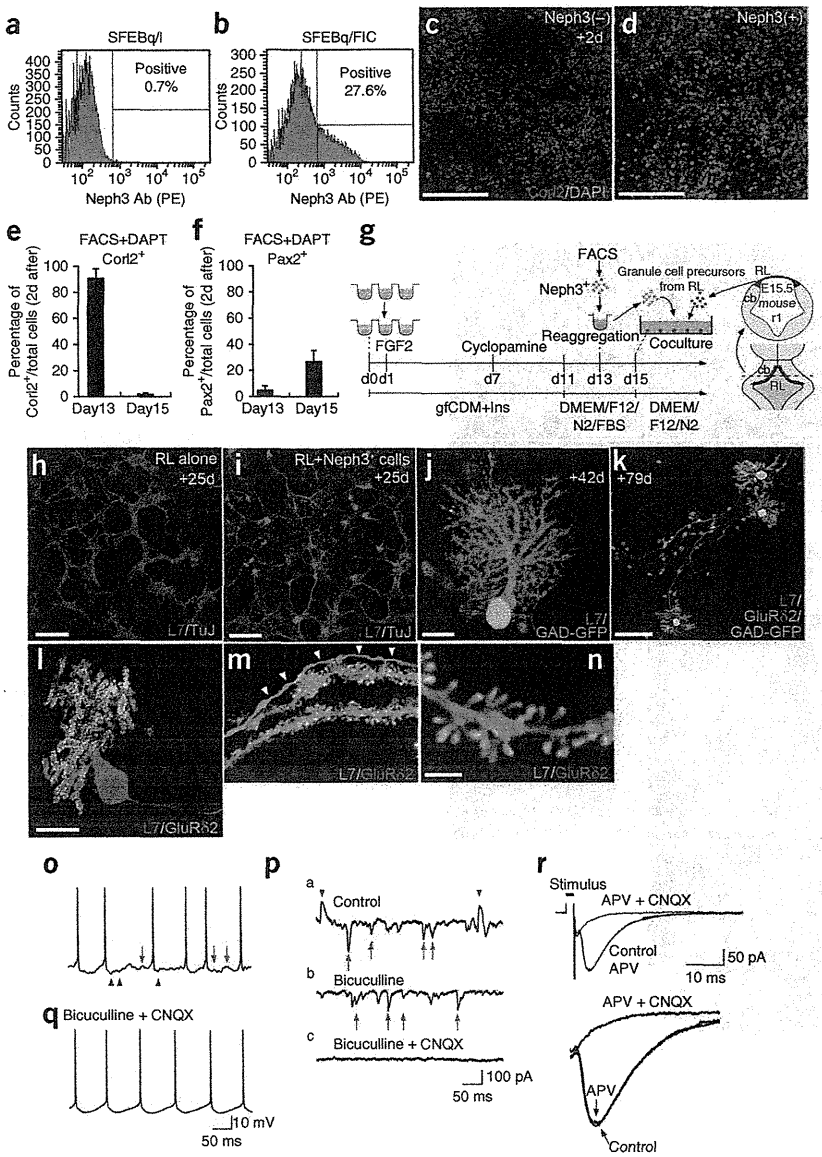

Figure 5 Neph3$^+$ progenitors on day 13 in SFEBq/FIC culture efficiently generate Purkinje cells with morphological and functional characteristics. (**a**,**b**) FACS analysis of ES cell aggregates on day 13 of SFEBq culture in the presence of insulin alone (**a**) or insulin, Fgf2 and cyclopamine (**b**). (**c**,**d**) Adhesion culture of Neph3-positive (**c**) and Neph3-negative (**d**) cells after FACS sorting, immunostained with Corl2. (**e**,**f**) Percentage of the cells expressing Corl2 (**e**) and Pax2 (**f**) in aggregates 2 days after FACS sorting and DAPT treatment on day 13 or 15 of SFEBq culture ($n = 56$ aggregates from 5 independent experiments). (**g**) Procedure for ES cell culture combined with FACS sorting and co–culture with mouse rhombic lip–derived cells. FACS-sorted cells were reaggregated on day 13, and dissociated and replated on day 15 along with granule cell precursors from the upper rhombic lip of E15.5 mice. (**h**,**i**) Control culture of rhombic lip–derived cells alone (**h**) or co–culture of rhombic lip–derived cells and FACS-sorted Neph3-positive ES–derived cells (**i**) on day 25 of co-culture, immunostained with antibody to L7. (**j**–**n**) Co-culture of FACS-sorted Neph3-positive cells with rhombic lip–derived cells on day 42 (**j**) and day 79 (**k**–**n**), immunostained with antibodies to L7 (**j**) and L7 plus GluRδ2 (**k**–**n**). Arrowheads in **m** indicate an axon. (**o**) Spontaneous synaptic potentials and action potentials. Arrows indicate presumptive excitatory postsynaptic potentials, and arrowheads indicate presumptive inhibitory postsynaptic potentials. (**p**) Spontaneous synaptic currents without (top) and with bicuculline (middle) or bicuculline and CNQX (bottom). Arrows indicate presumptive excitatory postsynaptic currents, and arrowheads indicate presumptive inhibitory postsynaptic currents. (**q**) Spontaneous action potentials without synaptic inputs. (**r**) Evoked excitatory postsynaptic current without or with AP5 or AP5 and CNQX. Each trace is an average of 5 traces. Scale bars: 200 μm (**c**,**d**,**h**,**i**); 25 μm (**j**,**l**); 100 μm (**k**); 2 μm (**n**). Error bars represent s.e.m.

figures (**Fig. 4l**) were predominantly found at or near the apical area. The nuclei of Ki67$^+$ and Ptf1a$^+$ cells were also localized in the inner zone close to the apical cavity (**Fig. 4m–o**). In contrast, most of the Corl2$^+$ nuclei were at least three to four cells away from the apex, and formed an outer zone that surrounded the Ptf1a$^+$ proliferative zone (**Fig. 4p,q**; day 15). These Corl2$^+$ cells were predominantly found in the outer zones of Neph3$^+$ rosettes (up to 58.8 ± 11.5% cells in the rosettes), but not in those of Neph3$^-$ rosettes (**Supplementary Fig. 4**).

We next performed a birth-dating comparison between the Corl2$^+$ (Purkinje) and Pax2$^+$ (non-Purkinje[30]) cell populations (these markers were mutually exclusive; **Supplementary Fig. 4**) using a pulse exposure to 5-ethynyl-2-deoxyuridine (EdU) (**Supplementary Fig. 4**). The number of Corl2$^+$ cells that incorporated EdU was significantly higher when the aggregates were exposed to EdU on day 13 than on day 15 or 16 (**Fig. 4r** and **Supplementary Fig. 4**). In contrast, the Pax2$^+$ (non-Purkinje) cell populations were more efficiently labeled by EdU on days 15 and 16 than on day 13 (10–17% of Pax2$^+$ cells were mitotic and Ki67$^+$ on day 16, as *in vivo*; **Fig. 4r**, **Supplementary Fig. 4** and data not shown). Most (>90%) of the Neph3$^+$ neural rosettes on day 13 were E-cadherin$^+$ (**Fig. 4m**), which marks the Purkinje-generating neuroepithelium, but by day 15 the E-cadherin expression in the Neph3$^+$ neural rosettes had substantially decreased (not shown). These findings are consistent with the *in vivo* neurogenesis, in that Purkinje cells are the first of the cerebellar cortical neurons to exit the cell cycle. These observations suggest that SFEBq/FIC-cultured cells recapitulate not only regional marker expression but also key temporal and spatial aspects of the *in vivo* development of Purkinje cells.

Mature Purkinje cells from purified progenitors

Taking advantage of the cell-surface localization of Neph3, we next used this early marker to select Purkinje cell progenitors by timed sorting. In fluorescence-activated cell sorting (FACS) analysis, 25–35% of the SFEBq/FIC cells on day 13 were strongly positive for Neph3 (**Fig. 5a,b**), and the purified Neph3$^+$ population generated a large number of Corl2$^+$ cells (82.7 ± 8.4% of total cells) in two

days. In contrast, only 3.1 ± 0.8% of the Neph3$^-$ cells became Corl2$^+$ (**Fig. 5c,d**). We next compared the content of Purkinje cell precursors among Neph3$^+$ progenitors sorted on different days in culture. After sorting, the cells were treated with DAPT to inhibit Notch and thereby promote neuronal differentiation, and cultured for two more days. The vast majority of Neph3$^+$ cells sorted on day 13 differentiated into Corl2$^+$ cells (>90%), and a minor population gave rise to Pax2$^+$ neurons (**Fig. 5e**). In contrast, more Neph3$^+$ cells sorted on day 15 differentiated into Pax2$^+$ neurons (27.1 ± 8.2%) than into Corl2$^+$ cells (5.3 ± 2.9%) (**Fig. 5f**; the DAPT treatment caused at least a two-fold increase in the percentage of Pax2$^+$ neurons; data not shown). Thus, in accordance with the birth-dating analysis, isolating the Neph3$^+$ progenitors on day 13 has proven to be an efficient way to enrich for ES cell–derived Purkinje cell progenitors.

In a conventional high-density neuronal culture, the purified Neph3$^+$ cells gradually died, and the surviving neurons failed to express late Purkinje cell markers such as L7 and Calbindin even two weeks later (data not shown). A similar observation was made with Neph3$^+$ cells purified from fetal cerebellar plate tissues[28] (E12.5), presumably because the appropriate trophic microenvironment could not be established in the purified cell population. To circumvent these problems, we co-cultured Neph3$^+$ cells with cerebellar granule cells, which promotes the maturation and survival of Purkinje cells *in vitro*[31] (we avoided DAPT treatment as it attenuated survival in long-term culture). In the presence of granule cells derived from the rhombic lip (**Fig. 5g**), the purified Neph3$^+$ cells survived and generated a large number of L7$^+$ Calbindin$^+$ PV$^+$ neurons (**Fig. 5h,i** and **Supplementary Fig. 5**) with characteristic, highly arborized dendrites (**Fig. 5j**). When cultured alone, the rhombic lip cells produced no L7$^+$ cells (**Fig. 5h**). Moreover, when we used Neph3$^+$ progenitors derived from *Gad67::GFP* (GAD-GFP) ES cells (>90% of these progenitors became GAD-GFP$^+$ after two days of dissociation culture) in the co-cultures, all of the L7$^+$ neurons expressed GFP (**Fig. 5j**; conversely, 38.2 ± 4.3% of the GFP$^+$ cells expressed L7$^+$). Furthermore, when the rhombic lip cells were isolated from GFP-transgenic mouse cerebella, no Corl2$^+$ or L7$^+$ cells generated from nonlabeled ES cells were GFP$^+$ (**Supplementary Fig. 5**), excluding the possibility of differentiation by cell fusion.

After long-term culture, each ES cell–derived Purkinje cell had dendrites with numerous, well-developed spines that expressed the Purkinje cell–specific glutamate receptor subunit GluRδ2 (**Fig. 5k–n**).

To investigate their functional properties, we performed whole-cell patch-clamp recording of the SFEBq/FIC-induced Purkinje cells after their maturation in co-culture with granule cells. Under current clamp, large Purkinje cells showed frequent action potentials (large spikes) and synaptic potentials (**Fig. 5o**). Voltage-clamp recordings (−50 mV; **Fig. 5p**) revealed that the inward currents (red) were CNQX sensitive, showing that they were AMPA receptor–mediated excitatory glutamatergic synaptic currents (generated by granule cell input[32] *in vivo*), whereas the outward currents (blue) were bicuculline sensitive, meaning that they were $GABA_A$ receptor–mediated inhibitory synaptic currents (presumably from other ES cell–derived GABAergic neurons including Purkinje cells). When these synaptic potentials were suppressed with CNQX and bicuculline, we recorded the repetitive firing of spontaneous action potentials (**Fig. 5q**; current clamp). Such intrinsic excitability is a characteristic of dissociated Purkinje cells[33].

Another intriguing characteristic of mature Purkinje cells is that the NMDA-type glutamate receptor makes no significant contribution to their synaptic responses[34], unlike many other neurons. In Mg^{2+}-free external solution, which unmasks synaptic currents mediated by the NMDA receptor (regardless of AMPA receptor activity), the NMDA receptor antagonist D(−)-2-amino-5-phosphonovaleric acid (AP5) did not significantly affect the amplitude or time course of inward synaptic currents (**Fig. 5r**), although these currents were suppressed completely by CNQX with AP5 (**Fig. 5r**) and by CNQX alone (data not shown). These results are consistent with the inward synaptic current of SFEBq/FIC-induced Purkinje cells being mediated predominantly by the AMPA receptor and not the NMDA receptor, again showing similar electrophysiological properties to native Purkinje cells in primary culture.

Orthotopic integration of ES cell–derived Purkinje cells

The postnatal cerebellum consists of the cortex and the DCN (**Supplementary Fig. 6**). The stratified cortex consists of the molecular layer, which contains parallel fibers and Purkinje cell dendrites, the Purkinje cell layer, the granule layer (containing granule cells), and the white matter (**Supplementary Fig. 6**).

For the transplantation study, Neph3$^+$ cells derived from GAD-GFP ES cells were sorted on day13, and then microinjected into the subventricular space of the E15.5 mouse cerebellar plate *in utero* (**Fig. 6a** and **Supplementary Fig. 6**; 10,000 cells per fetus). The majority of grafted GAD-GFP$^+$ neurons found in the host cerebella expressed Calbindin and L7 at 1 and 4 weeks after transplantation (**Fig. 6b–d** and data not shown; for example, 87.3 ± 4.2% of GAD-GFP$^+$ cells were L7$^+$ at the 4-week point; **Fig. 6e**; the ratio of the surviving GFP$^+$ cells per the total injected cells was ~3%; **Supplementary Fig. 6**), indicating that the ES cell–derived purified precursors differentiated into mature Purkinje cells *in vivo*. This was unlikely to be due to fusion with host cells, as we found no GFP labeling in grafted Purkinje cells generated from red fluorescent protein (RFP)-labeled ES cells (not carrying GFP), when we used the L7-GFP mouse as a host (five mice, each containing >200 grafted Purkinje cells; **Supplementary Fig. 6**). Most of the GAD-GFP$^+$ neurons were located in the Purkinje cell layer (**Fig. 6b–d,f**), suggesting that the ES cell–derived Purkinje cell precursors could undergo orthotopic integration.

Most of the integrated grafted Purkinje cells (>90%, 4 weeks after transplantation) showed normal cell polarity, and had well-developed dendrites growing outward in the molecular layer (**Fig. 6d,g**). High-resolution confocal imaging showed that their primary dendrites frequently received multiple VGluT2$^+$ patches (in a string-of-beads appearance; **Fig. 6h,i**), which reflect the presynaptic inputs of the climbing fibers[35]. In addition, in the periphery of the dendrites, the GluRδ2$^+$ spines were closely associated with the localization of cerebellin (Cbln1), which is specifically found at the presynaptic termini of parallel fibers *in vivo*[36,37] (**Fig. 6j–l**). The grafted Purkinje cells had a long axon extending through the granule layer (**Fig. 6g** and **Supplementary Fig. 6**) and white matter toward the DCN (**Supplementary Fig. 6**).

The DCN contains large (magnocellular) projection neurons that express SMI-32 (a glutamatergic marker; **Supplementary Fig. 6**) and small SMI-32$^-$ neurons (arrows in **Supplementary Fig. 6**). The GAD-GFP axonal terminals from the graft-derived L7$^+$ neurons extended to the DCN in 15–45% of the grafted cerebella (**Fig. 6m–o**), where they formed large synaptophysin$^+$ synaptic boutons that were found preferentially on the soma or the proximal dendritic roots of SMI-32$^+$ magnocellular DCN neurons (**Fig. 6m–o**).

This projection of Purkinje cell axons onto the magnocellular DCN somata is characteristic of the normal DCN[38] (**Supplementary Fig. 6**). A quantitative comparison showed that L7 axons from both endogenous and ES cell–derived Purkinje cells terminated

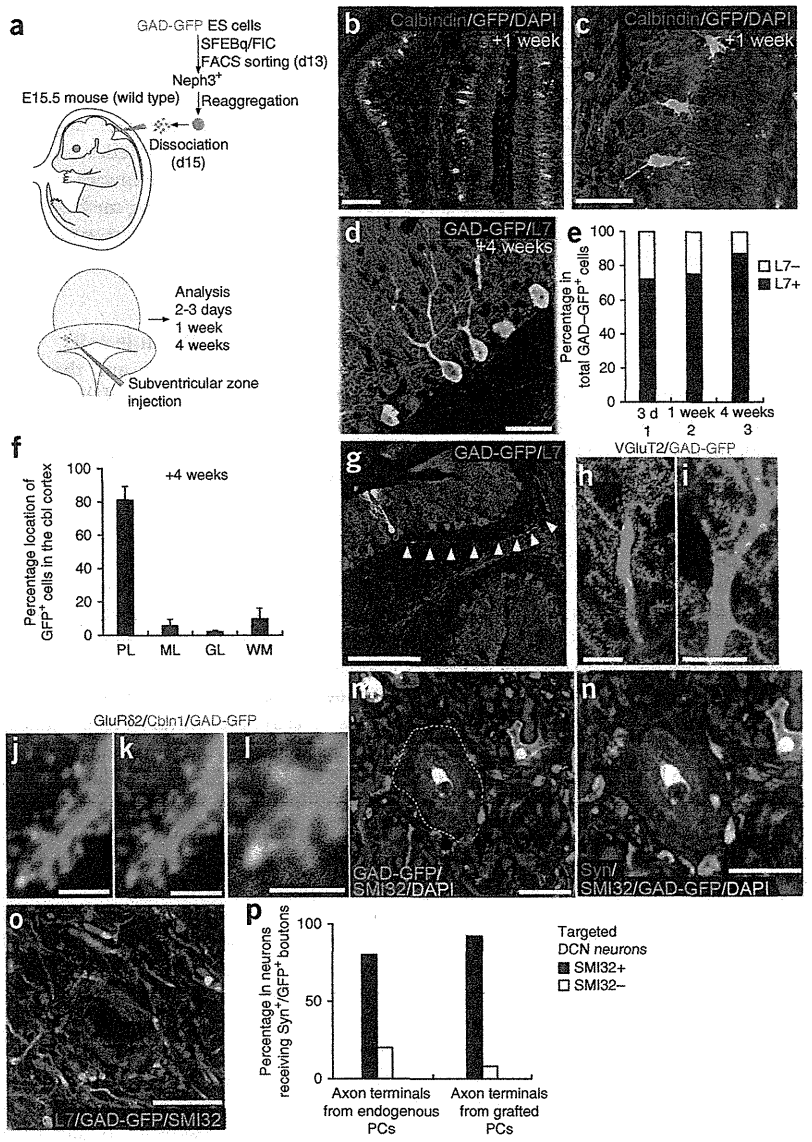

Figure 6 Orthotopic integration of ES cell–derived Purkinje cells into the cerebellum. **(a)** Schematic diagram of the method for *in utero* transplantation. **(b–d)** Integration of multiple grafted GFP$^+$ cells into the Purkinje cell layer of the host cerebellum. Immunostaining showed that grafted GFP$^+$ cells expressed calbindin (**b**,**c**) and L7 (**d**) at 1 week (**b**,**c**) and 4 weeks (**d**) after transplantation. **(e)** Percentage of GAD-GFP$^+$ neurons expressing L7 in the cerebellar plate on the indicated days after transplantation (3 mice each). **(f)** Percentage of integrated GFP$^+$ cells in each layer of the cerebellar cortex (5 mice). **(g)** Integration of a grafted GFP$^+$ cell with proper polarity. The GFP$^+$ axon (arrowheads) extends in the white matter along other L7$^+$ axons. **(h,i)** Confocal images of grafted GAD-GFP$^+$ dendrites. Puncta positive for the glutamate transporter VGluT2 were seen along the dendritic shafts of GFP$^+$ neurons (**h**, distal; **i**, proximal portion of dendrite). **(j–l)** High-magnification confocal images of grafted GAD-GFP$^+$ dendritic spines, immunostained for GluRδ2 (**j**), Cbln1 (**k**) and GluRδ2 + Cbln1 (**l**). **(m–o)** Section of an SMI-32$^+$ large glutamatergic DCN neuron. Graft-derived GAD-GFP$^+$ axons terminate at the soma and express synaptophysin (**n**; at their terminal boutons) and L7 (**o**). **(p)** Percentage of neurons surrounded by synaptophysin$^+$ GFP$^+$ boutons in the DCN. The majority of synaptophysin$^+$ L7-GFP$^+$ axons terminated on SMI-32$^+$ large glutamatergic neurons (closed column) in L7-GFP mice (left; 3 mice). Similarly, GAD-GFP$^+$ axons in grafted mice terminated predominantly on SMI-32$^+$ neurons (right; 6 mice). Scale bars: 100 μm (**b**); 50 μm (**c**,**d**); 200 μm (**g**); 10 μm (**h**,**i**,**m–o**); 2.5 μm (**j**,**k**); 2 μm (**l**). Error bars represent s.e.m.

predominantly on magnocellular SMI-32$^+$ DCN neurons, rather than on small SMI-32$^-$ ones (**Fig. 6p**; analysis based on the location of L7$^+$/synptophysin$^+$ boutons). Together, these findings show that ES cell–derived Purkinje cells can integrate orthotopically, project their axons to the correct DCN targets and form apparently normal synaptic connections *in vivo*.

DISCUSSION

In vitro cerebellar development by self-induction

Making the best use of the emerging knowledge on early cerebellar development[4,5,25,28], we successfully recapitulated the *in vivo* microenvironments of the cerebellum's developmental field in ES cell culture. Our three-step method (**Supplementary Fig. 5**) produced a substantial improvement (up to ~30-fold) over the previously reported frequency of Purkinje cell generation[18–20].

Each specification step is highly efficient and reasonably mimics the *in vivo* developmental process. For instance, >80% of the SFEBq/FI-cultured ES cells expressed En2 in the MHB-region specification step (**Fig. 1h**), and >70% of those were of the isthmus/rhombomere 1 type. Furthermore, 75% of the neuroepithelial rosettes were positive for Neph3$^+$/Ptf1a$^+$ (**Supplementary Fig. 4**). Following FACS sorting, around 90% of the Neph3$^+$ progenitors differentiated into Corl2$^+$ Purkinje cell precursors in 2 days *in vitro* (**Fig. 5e**).

The selective induction of En2$^+$ progenitors (which are present only in a small region of the developing brain *in vivo*) was unexpected, given that it was triggered by only a simple and transient treatment with Fgf2 in the presence of insulin (**Fig. 1i–l**). We infer that this phenomenon reflects a special characteristic of MHB development, involving self-inductive regulation. One reasonable interpretation is that the combination of two weak caudalizing signals (Fgf2 and insulin) was just sufficient to 'prepattern' the aggregates for a broad mid-hindbrain regionalization without interfering with the endogenous self-inductive program mediated by signals from the isthmic organizer. Subsequently, endogenous Wnt1 and Fgf8 signals (and related signals) could have formed a robust self-inductive system that led to MHB development and the concurrent generation of the appropriate cell types for the neighboring tissues (**Supplementary Fig. 1**). The existence of such prepatterning and self-development was also supported by a previous explant study showing that the embryonic neuroectoderm at the mid-streak stage is already prepatterned for tissue-autonomous *En2* expression, far before its onset at the early somite stage[39].

In this view, it is reasonable that the direct application of exogenous Fgf8 and Wnt1, which could perturb their endogenous signaling counterparts, could have resulted in relatively less efficient induction of En2, unlike the simple Fgf2 treatment, which is thought to cause little interference with the subsequent self-inductive processes. The use of chemically defined medium was probably also helpful in this highly selective differentiation, because it avoided undefined factors that could complicate these signaling interactions. Indeed, the addition of KSR (knockout serum replacement), which is commonly used in ES cell culture, reduced the efficiency of En2 induction (data not shown). In addition, selective neural differentiation in SFEBq culture occurs without obvious mesodermal differentiation[21,22] (even in the presence of Fgf); this might also help to simplify the cellular interactions for the self-inductive development of the MHB.

Generally speaking, in the developing brain, the rostral-caudal determination occurs earlier than decisive dorsal-ventral patterning. In our system, the dorsal specification into the cerebellar plate identity was achieved by using the hedgehog inhibitor cyclopamine (**Fig. 2**) from day 7. This method of passive dorsal specification proved to be better for the generation of Purkinje cell progenitors than was active dorsalization using the strong dorsalizing factor BMP4, which preferentially induced the differentiation of glutamatergic Math1$^+$ granule cells and Tbr1$^+$ DCN neurons (**Fig. 2i,m**). This differential effect can be explained, at least in part, by the fact that Purkinje cells arise from a broad area of the dorsal (alar) plate of rhombomere 1, whereas granule cells and DCN neurons originate exclusively from the dorsal-most tip of the neural tube. In accordance with this interpretation, treatment with both cyclopamine and BMP4 was less effective for inducing Purkinje cell progenitors than cyclopamine treatment alone (**Fig. 2v**, lanes 4 and 5).

Remaining questions and future applications

SFEBq/FIC-generated cerebellar progenitors were efficiently isolated by FACS using an anti-Neph3 antibody. The day of culture on which cells were sorted was a key parameter for obtaining Purkinje cell–generating progenitors. Progenitors purified from day 13 in culture (but not day 15 in culture) differentiated into Corl2$^+$ Purkinje cell precursors (postmitotic) at high frequency in dissociation culture (~90%; **Fig. 5d,e**). In contrast, the generation of Pax2$^+$ cells (which generate non-Purkinje GABAergic neurons such as Golgi cells; **Supplementary Fig. 5**) from Neph3$^+$ progenitors was more efficient with cells sorted on day 5 than on day 13. This differential relationship was consistent with our birth-dating analysis (**Fig. 4r**) and the expression profile of E-cadherin (which is expressed more strongly on day 13 than on day 15) as well as with the timing of cerebellar development *in vivo*.

In a co-culture system of sorted Neph3$^+$ progenitors with rhombic lip–derived granule cells, ~40% of the ES cell–derived GABAergic neurons (GAD-GFP$^+$) were L7$^+$ Purkinje cells (**Fig. 5i**). Although this percentage, seen after long-term co-culture (25 d), was fairly remarkable, it was still lower (about by half) than the percentage (83–90%) of Corl2$^+$ precursors generated from Neph3$^+$ progenitors in dissociation culture 2 days after sorting (**Fig. 5d**). This reduced efficiency might reflect the moderate dilution of the Purkinje cell population by non-Purkinje GABAergic neurons that were also generated from Neph3$^+$ progenitors after the Purkinje cell production was finished (also note that a portion of Pax2$^+$ cells are initially mitotic; **Supplementary Fig. 4**). The contribution of biased apoptosis remains elusive, as our preliminary study detected only low percentages of ES cell–derived apoptotic cells (<1% positive for active caspase 3) regardless of L7 expression (not shown).

Purkinje cell loss is associated with cerebellar degeneration, particularly of the SCA6 type[40]. Unfortunately, cell transplantation is hindered by a technical issue: exogenous cerebellar neurons have historically had low integration efficiency. In this study, we injected Neph3$^+$ progenitors into the cerebellar plate of E15.5 mice. Four weeks later, the numbers of surviving grafted GAD-GFP$^+$ neurons was typically ~3% of the grafted neurons, although most (>90%) of the integrated neurons were L7$^+$ Purkinje cells. We also found low integration efficiency in our grafting study of endogenous cerebellar progenitors from GAD-GFP mice (<2–3%; **Supplementary Fig. 6**), indicating that this problem is not limited to the ES cell–derived cells. The integration efficacy was even lower when cells were transplanted into the postnatal cerebellum (postnatal day 3 to week 8; **Supplementary Fig. 6**), consistent with previous studies[41]. In contrast to the fetal transplantation, GAD-GFP$^+$ cells that were injected postnatally did not integrate into the postnatal cerebellar cortex but mostly stayed in the white matter, and did not express L7 or calbindin (**Supplementary Fig. 6**). We have attempted to improve the neuronal integration in the adult mouse by using a cerebellar degeneration model line[42], but so far the integration rate remains low, suggesting that it is not simply due to the lack of a niche or free space. We infer that successful cellular integration during the early period after transplantation is an important decisive factor, as both the number of surviving GAD-GFP$^+$ cells and the percentage of L7$^+$ cells among them were much the same a few days and four weeks after grafting (**Fig. 6e** and **Supplementary Fig. 6**). In the future, intensive efforts to create permissive *in vivo* conditions for the improved survival of grafted cerebellar neurons will be essential for the functional recovery of cerebellar degeneration by cell replacement.

METHODS

Methods and any associated references are available in the online version of the paper at http://www.nature.com/natureneuroscience/.

Note: Supplementary information is available on the Nature Neuroscience website.

ACKNOWLEDGMENTS

We thank H. Enomoto and M. Eiraku for comments, T. Wataya for help in tissue preparation and members of the Sasai laboratory for discussion and advice. This work was supported by grants-in-aid from the Ministry of Education, Culture, Sports, Science and Technology (Japan), the Kobe Cluster Project, the Leading Project (Y.S.) and the National Center of Neurology and Psychiatry (K.M.).

AUTHOR CONTRIBUTIONS

K.M. performed the experiments that comprise the main body of this work. A.N. assisted with cell culture and histology. Y.O. and E.M. contributed to the FACS analysis. H.M. and T.H. performed electrophysiological analysis. S.H. and A.K. contributed to the ataxia model mouse analysis. K.O. and Y.Y. provided GAD-GFP transgenic mice. Y.S. wrote the manuscript and designed the experiments with K.M.

COMPETING FINANCIAL INTERESTS

The authors declare no competing financial interests.

Published online at http://www.nature.com/natureneuroscience/.
Reprints and permissions information is available online at http://www.nature.com/reprintsandpermissions/.

1. Wingate, R.J.T. & Hatten, M.E. The role of the rhombic lip in avian cerebellum development. *Development* **126**, 4395–4404 (1999).
2. Zervas, M., Milet, S., Ahn, S. & Joyner, A.L. Cell behavior and genetic lineage of the mesencephalon and rhombomere 1. *Neuron* **43**, 345–357 (2004).
3. Park, C., Falls, W., Finger, J.H., Longo-Guess, C.M. & Ackerman, S.L. Deletion in Catna 2, encoding alpha N-catenin, causes cerebellar and hippocampal lamination defects and impaired startle modulation. *Nat. Genet.* **31**, 279–284 (2002).
4. Hoshino, M. *et al. Ptf1a*, a HLH transcriptional gene, defines GABAergic neuronal fates in cerebellum. *Neuron* **47**, 201–213 (2005).

5. Machold, R. & Fishell, G. Math1 is expressed in temporally discrete pools of cerebellar rhombic-lip neural progenitors. *Neuron* **48**, 17–24 (2005).
6. Ben-Arie, N. *et al. Math1* is essential for genesis of cerebellar granule neurons. *Nature* **390**, 169–172 (1997).
7. Fink, A.J. *et al.* Development of the deep cerebellar nuclei: transcription factors and cell migration from the rhombic lip. *J. Neurosci.* **26**, 3066–3076 (2006).
8. Joyner, A.L. *Engrailed*, *Wnt* and *Pax* genes regulate midbrain-hindbrain development. *Trends Genet.* **12**, 15–20 (1996).
9. Crossley, P.H., Martinez, S. & Martin, G. Midbrain development induced by FGF8 in the chick embryo. *Nature* **380**, 66–68 (1996).
10. Liu, A., Losos, K. & Joyner, A.L. FGF8 can activate *Gbx2* and transform regions of the rostral mouse into a hindbrain fate. *Development* **126**, 4827–4838 (1999).
11. Martinez, S., Crossley, P.H., Cobos, I., Rubenstein, J.L.R. & Martin, G.R. FGF8 induces formation of an ectopic isthmic organizer and isthmocerebellar development via repressive effect on *Otx2* expression. *Development* **126**, 1189–1200 (1999).
12. Meyers, E.N., Lewandoski, M. & Martin, G.R. An *Fgf8* mutant allelic series generated by Cre- and Flp-mediated recombination. *Nat. Genet.* **18**, 136–141 (1998).
13. Sato, T., Araki, I. & Nakamura, H. Inductive signal and tissue responsiveness defining the tectum and the cerebellum. *Development* **128**, 2461–2469 (2001).
14. Thomas, K.R. & Capecchi, M.R. Targeted disruption of the murine int-1 proto-oncogene resulting in severe abnormalities in midbrain and cerebellar development. *Nature* **346**, 847–850 (1990).
15. McMahon, A.P., Joyner, A.L., Bradley, A. & McMahon, J.A. The midbrain-hindbrain phenotype of *Wnt-1*$^{-}$/*Wnt-1*$^{-}$ mice results from stepwise deletion of *engrailed*-expressing cells by 9.5 days postcitum. *Cell* **69**, 581–595 (1992).
16. Simeone, A. Positioning the isthmic organizer where *Otx2* and *Gbx2* meet. *Trends Genet.* **16**, 237–240 (2000).
17. Watanabe, K. *et al.* Directed differentiation of telencephalic precursors from embryonic stem cells. *Nat. Neurosci.* **8**, 288–296 (2005).
18. Su, H.-L. *et al.* Generation of cerebellar neuron precursors from embryonic stem cells. *Dev. Biol.* **290**, 287–296 (2006).
19. Salero, E. & Hatten, M.E. Differentiation of ES cells into cerebellar neurons. *Proc. Natl. Acad. Sci. USA* **104**, 2997–3002 (2007).
20. Tao, O. *et al.* Efficient generation of mature cerebellar Purkinje cells from mouse embryonic stem cells. *J. Neurosci. Res.* **88**, 234–247 (2010).
21. Wataya, T. *et al.* Minimization of exogenous signals in ES cell culture induces rostral hypothalamic differentiation. *Proc. Natl. Acad. Sci. USA* **105**, 11796–11801 (2008).
22. Eiraku, M. *et al.* Self-organized formation of polarized cortical tissues from ESCs and its active manipulation by extrinsic signals. *Cell Stem Cell* **3**, 519–532 (2008).
23. Davis, C.A. & Joyner, A.L. Expression patterns of the homeo box-containing genes *En-1* and *En-2* and the proto-oncogene *int-1* diverge during mouse development. *Genes Dev.* **2**, 1736–1744 (1988).
24. Ye, W., Shimamura, K., Rubenstein, J.L.R., Hynes, M.A. & Rosenthal, A. Fgf and Shh signals control dopaminergic cell fate in the anterior neural plate. *Cell* **93**, 755–766 (1998).
25. Minaki, Y., Nakatani, T., Mizuhara, E., Inoue, T. & Ono, Y. Identification of a novel transcriptional co-repressor, Corl2, as a cerebellar Purkinje cell–selective marker. *Gene Expr. Patterns* **8**, 418–423 (2008).
26. Alder, J., Lee, K.J., Jessel, T.M. & Hatten, M.E. Generation of cerebellar granule neurons *in vivo* by transplantation of BMP-treated neural progenitor cells. *Nat. Neurosci.* **2**, 535–540 (1999).
27. Wilson, L. & Maden, M. The mechanisms of dorsoventral patterning in the vertebrate neural tube. *Dev. Biol.* **282**, 1–13 (2005).
28. Mizuhara, E. *et al.* Purkinje cells originate from cerebellar ventricular zone progenitors positive for Neph3 and E-cadherin. *Dev. Biol.* **338**, 202–214 (2010).
29. Altman, J. & Bayer, S.A. *Development of the Cerebellar System in Relation to its Evolution, Structures and Functions* (CRC Press, Boca Raton, Florida, 1997).
30. Maricich, S.M. & Herrup, K. Pax2 expression defines a subset of GABAergic interneurons and their precursors in the developing murine cerebellum. *J. Neurobiol.* **41**, 281–294 (1999).
31. Baptista, C.A., Hatten, M.E., Blazeski, R. & Mason, C.A. Cell-cell interactions influence survival and differentiation of purified Purkinje cells *in vitro*. *Neuron* **12**, 243–260 (1994).
32. Hirano, T. & Kasono, K. Spatial distribution of and inhibitory synapses on a Purkinje cell in a rat cerebellar culture. *J. Neurophysiol.* **70**, 1316–1325 (1993).
33. Raman, I.M. & Bean, B.P. Ionic currents underlying spontaneous action potentials in isolated cerebellar Purkinje neurons. *J. Neurosci.* **19**, 1663–1674 (1999).
34. Hirano, T. & Hagiwara, S. Synaptic transmission between rat cerebellar granule and Purkinje cells in dissociated cell culture: effects of excitatory-amino acid transmitter antagonists. *Proc. Natl. Acad. Sci. USA* **85**, 934–938 (1988).
35. Miyazaki, T., Fukaya, M., Shimizu, H. & Watanabe, M. Subtype switching of vesicular glutamate transporters at parallel fibre–Purkinje cell synapses in developing mouse cerebellum. *Eur. J. Neurosci.* **17**, 2563–2572 (2003).
36. Matsuda, K. *et al.* Cbln1 is a ligand for an orphan glutamate receptor delta2, a bidirectional synapses organizer. *Science* **328**, 363–368 (2010).
37. Uemura, T. *et al.* Trans-synaptic interaction of GluRδ2 and Neurexin through Cbln1 mediates synapse formation in the cerebellum. *Cell* **141**, 1068–1079 (2010).
38. Garin, N. & Escher, G. The development of inhibitory synaptic specialization in the mouse deep cerebellar nuclei. *Neuroscience* **105**, 431–441 (2001).
39. Ang, S.L. & Rossant, J. Anterior mesendoderm induces mouse engrailed genes in explant cultures. *Development* **118**, 139–149 (1993).
40. Frontali, M. Spinocerebellar ataxia type 6: Channelopathy or glutamine repeat disorder? *Brain Res. Bull.* **56**, 227–231 (2001).
41. Cendelin, J.I., Korelusova, I. & Vozeh, F. The effect of cerebellar transplantation and enforced physical activity on motor skills and spatial learning in adult lurcher mutant mice. *Cerebellum* **8**, 35–45 (2009).
42. Ikeda, H. *et al.* Expanded polyglutamine in the Machado-Joseph disease protein induces cell death *in vitro* and *in vivo*. *Nat. Genet.* **13**, 196–202 (1996).

ONLINE METHODS

ES cell culture. Mouse ES cells (EB5) were maintained as described[17]. To generate GAD67-GFP knock-in ES cells, we obtained E3.5 blastocysts from pregnant female 129x1/SvJ mice mated with heterozygous GAD67-GFP (neo) mice[43] and subjected them to ES cell derivation on mouse embryonic fibroblasts. For SFEBq culture, ES cells were dissociated to single cells in 0.25% trypsin-EDTA and quickly reaggregated in differentiation medium (3,000 cells per 150 μl per well) in 96-well low-cell-adhesion plates (Lipidure Coat, NOF). The basal differentiation medium used during days 0–11 was gfCDM (modified from ref. 44), consisting of Isocove's modified Dulbecco's medium/Ham's F-12 1:1, chemically defined lipid concentrate, penicillin/streptomycin, monothioglycerol (450 μM), apo-transferrin (15 μg ml^{-1}) and crystallization-purified BSA (5 mg ml^{-1}, >99%, Sigma). The medium was supplemented with insulin (7 μg ml^{-1}) on day 0 (the starting day of differentiation culture) unless otherwise noted. Recombinant proteins were purchased from R&D Systems. Cyclopamine was purchased from Toronto Research Chemicals.

Immunohistochemistry. Immunohistochemistry was performed as described[17]. For quantitative analysis, 16–24 aggregates were examined for each experiment, which was repeated at least five times. Antibodies to the following proteins were used at the indicated dilutions: En2 (goat 1:100, Santa Cruz), Otx2 (goat 1:100, Santa Cruz, rabbit 1:100, Abcam), Pax2 (rabbit 1:200, Zymed, mouse 1:1,000, Abnova), Tbr1 (rabbit 1:1,000, Chemicon), 5HT (rabbit 1:1,000, Protos), tyrosine hydroxylase (sheep 1:100, Chemicon), Lhx5 (goat 1:100, Santa Cruz), Calbindin (mouse 1:1,000, Swant, goat 1:100, SantaCruz), Neph3 (Kirrel2) (goat 1:2,000, R&D Systems), E-cadherin (rat 1:50, Takara), N-cadherin (mouse 1:1,000, BD Transduction), Ki67 (mouse 1:200, BD Pharmingen), aPKC (PKCζ, rabbit 1:100, Santa Cruz), pH3 (mouse 1:500, Cell Signaling), GluRδ2 (goat 1:100, Santa Cruz), Synaptophysin (rabbit 1:400, Zymed), SMI-32 (mouse 1:200, Covance), Meis1/2 (goat 1:100, Santa Cruz), Parvalbumin (mouse 1:2,000, Sigma), VGluT2 (guinea pig 1:1,000, Chemicon), Cbln1 (rabbit 1:200, Abcam), Neurogranin (rabbit 1:1,000, Chemicon), Corl2 (ref. 25) (rabbit 1:200), Ptf1a[25] (hamster 1:2), Neph3 (ref. 28) (hamster 1:100), Math1 (ref. 18) (guinea pig 1:3,000), L7 (ref. 18) (rabbit 1:5,000). DAPI was used for counterstaining the nuclei (Molecular Probes). NeuroTrace was used for Nissl's staining (Molecular Probes). NEO-STEM was used for labeling of grafted cells (Biterials). Stained sections were analyzed with LSM710 confocal microscope (Zeiss). Images were assembled by Adobe Photoshop CS2.

Quantitative PCR. Quantitative PCR was performed using the 7500 Fast Real Time PCR System (Applied Biosystems) and data were normalized to GAPDH expression. The primers used for qPCR are listed in **Supplementary Table 1**. The values shown on graphs represent the mean ± s.e.m. For quantitative analysis, 24–48 aggregates were examined for each experiment, which was repeated at least five times.

Neuronal differentiation culture. For the SFEBq/FIC culture, Fgf2 (20 ng ml^{-1}) was added on day 1, and cyclopamine (10 μM) on day 7 to the insulin-containing gfCDM medium (**Fig. 3a**). On day 11, the cell aggregates were transferred to a collagen-coated membrane (Transwell-COL, Corning) in DMEM/F12/N2/10%FBS supplemented with 7 g l^{-1} glucose.

FACS sorting. For FACS analysis, cells were counted with FACSAria (Becton Dickinson), and the data were analyzed with the FACSDiva software (Becton Dickinson). The cells were dissociated to single cells by Accumax (Chemicon) treatment and analyzed at 4 °C. For the Neph3$^+$ cell isolation experiments, the cells were dissociated with Accumax on day 13 or day 15 and filtered through a Cell Strainer (BD Biosciences). The cells were then incubated with an anti-Neph3 monoclonal antibody and labeled with a PE-conjugated secondary antibody (BD Biosciences). Sorted cells were collected in ice-cold DMEM/F12/N2/10%FCS and quickly reaggregated in low-cell-adhesion 96-well culture plates (1×10^4 cells per well). Sorted Neph3-positive and -negative cells were reanalyzed by FACS and qPCR to confirm the quality of sorting. For forced neuronal differentiation, DAPT (10 μM) was added after the sorting.

Birth-dating analysis. For the *in vitro* birth-dating analysis, aggregates were treated with EdU (5 μg ml^{-1}, Invitrogen) on days 10, 11, 12, 13, 14, 15 or 16, and rinsed with medium after 12 h, to remove the EdU. On day 19, the cell aggregates were fixed and cryosectioned. Sections were immunostained for EdU and each cerebellar neuron marker. The percentage of EdU$^+$ cells that expressed Corl2 or Pax2 was quantified. For the quantification, 16–24 aggregates were examined for each experiment, which was repeated at least three times.

Dissociation neuronal coculture. For cocultures of granule cells with cerebellar Purkinje cells, the upper rhombic lip (rhombomere 1) was strictly dissected from E15.5 mice and dissociated with Accumax. The cells were sorted on day 13 *in vitro*, reaggregated, and the reaggregated Neph3$^+$ cells were dissociated again on day 15 (2 days after the sorting). The sorted cells were mixed with the dissociated mice rhombic lip cells at a ratio of 1:3, and the mixed cells were plated onto poly-D-lysine/laminin-coated cover glasses at a density of 2×10^5 cells per 100 μl per cm^2 in DMEM/F12/N2/10%FBS/penicillin-streptomycin. After a 3-h incubation in a CO_2 incubator, culture medium was added to each dish to reduce the concentration of serum. The culture medium consisted of DMEM/F12/N2 supplemented with tri-iodothyronine (T3, 0.5 ng ml^{-1}). The cells were fed once a week by replacing half of the old medium with fresh medium that was supplemented with BSA (100 μg ml^{-1}) and cytosine arabinoside (Ara-C, 4 μM)[45].

Electrophysiological analysis. Electrophysiological analysis was performed as described[34]. Whole-cell patch-clamp recordings were made from dissociated cultured cells at room temperature (~21–25 °C). The extracellular bath solution consisted of (mM): 145 NaCl, 5 KOH, 2 $CaCl_2$, 1 $MgCl_2$, 10 HEPES and 10 glucose (pH 7.3). The patch pipette solution consisted of (mM): 140 D-glucuronic acid, 7 KCl, 155 KOH, 5 EGTA, 10 HEPES, 2 Mg-ATP and 0.2 Na-GTP. The membrane potential was held at −70 mV unless otherwise stated. The junction potential was offset. The signal was filtered at 2.9 kHz and digitized at 20 kHz. Only recordings with an input resistance of more than 100 MΩ and a series resistance of <25 MΩ were accepted. In some experiments, bicuculline (20 μM) or CNQX (10 μM) was applied to the bath solution. To record evoked EPSCs, a voltage pulse (10 V, 2 ms) was applied to the soma of a granule cell through a glass electrode in a bath solution lacking Mg^{2+} and including 1 μM glycine. In this experiment, QX-314 (5 mM) was added to the internal solution to block action potentials. AP5 (100 μM) and CNQX were used to suppress AMPA-type and NMDA-type glutamate receptor–mediated currents, respectively. When synaptic potentials were suppressed, the resting membrane potential of the ES cell–derived Purkinje cells was −57.5 ± 3.0 mV, and the amplitude, half-height width and frequency of the action potentials were 52.4 ± 7.9 mV, 1.8 ± 0.8 ms and 8.4 ± 4.5 Hz, respectively.

***In utero* injection.** The transplanted cells were *GAD67-GFP* ES cells that were prepared by FACS sorting on day 13. The Neph3$^+$ cells were aggregated *in vitro* for 2 days, and then dispersed with Accumax (no DAPT treatment was given, as it was less beneficial for long-term survival). To perform the transplantation, pregnant mice (on day 15.5 of gestation; the cerebellar anlage at this stage contained 8.2–9.1 × 10^4 cells, and 1.8–2.0 × 10^4 of these cells were Neph3$^+$ by flow cytometry) were deeply anesthetized with an intraperitoneal injection of sodium pentobarbital. The uterine horns were exposed, and 2 μl of cell suspension (5×10^3 cells per μl) was injected into the cerebellar plate and throughout the fourth ventricle of each embryo with a glass micropipette. The cerebellum was dissected at indicated time-points, sectioned at a 50-μm thickness, and the sections were immunostained.

Mice. Female 129x1/SvJ mice, pregnant C57BL/6-Tg(CAG-EGFP) mice, C57BL/6 and ICR mice were purchased from Nihon-SLC. B6;FVB-Tg(Pcp2-EGFP)2Yuza/J mice (described as L7-GFP mice) were obtained from Jackson Laboratory[46].

43. Tamamaki, N. *et al.* Green fluorescent protein expression and colocalization with carletinin, parvalbumin, and somatostatin in the GAD67-GFP knock-in mice. *J. Comp. Neurol.* **467**, 60–79 (2003).
44. Johansson, B.M. & Wiles, M.V. Evidence of involvement of activin A and bone morphogenetic protein 4 in mammalian mesoderm and hematopoietic development. *Mol. Cell. Biol.* **15**, 141–151 (1995).
45. Tabata, T. *et al.* A reliable method for dissociated mouse cerebellar cells enriched for Purkinje neurons. *J. Neurosci. Methods* **104**, 45–53 (2000).
46. Tomomura, M., Rice, D.S., Morgan, J.I. & Yuzaki, M. Purification of Purkinje cells by fluorescence-activated cell sorting from transgenic mice that express green fluorescent protein. *Eur. J. Neurosci.* **14**, 57–63 (2001).

Interaction of ataxin-3 with huntingtin-associated protein 1 through Josephin domain

Yukio Takeshita[a,b], Ryutaro Fujinaga[a], Keiji Kokubu[a], Md. Nabiul Islam[a], Mir Rubayet Jahan[a], Akie Yanai[a], Akira Kakizuka[c] and Koh Shinoda[a]

Huntingtin-associated protein 1 (HAP1) is an essential component of the stigmoid body (STB) and known as a possible neuroprotective interactor with causative proteins for Huntington's disease, spinal and bulbar muscular atrophy, spinocerebellar ataxia type 17 (SCA17), and Joubert syndrome. To clarify what other causative molecules HAP1/STB could interact with, we cloned normal causative genes for several neural disorders from human brain RNA library and evaluated their subcellular interaction with HAP1/STB by immunocytochemistry and immunoprecipitation after cotransfection into Neuro2a cells. The results clearly showed that HAP1/STB interacts with the normal ataxin-3 through Josephin domain and polyglutamine-expanded mutants derived from SCA3 as well. The findings suggest that HAP1/STB could modify the physiological function of normal ataxin-3 and pathogenesis of SCA3 attributable to the mutant ataxin-3. *NeuroReport* **22:232–238 © 2011 Wolters Kluwer Health | Lippincott Williams & Wilkins.**

NeuroReport 2011, 22:232–238

Keywords: Machado-Joseph disease, Huntington's disease, Triplet Repeat, Neurode generation, spinocerebellar ataxia type 3, stigmoid body

[a]Department of Neuroscience, Yamaguchi Graduate University School of Medicine, Ube, Yamaguchi, Japan, [b]The Japan Society for the Promotion of science, Tokyo and [c]Laboratory of Functional Biology, Graduate School of Biostudies, Kyoto University, Kyoto, Japan

Correspondence to Dr Koh Shinoda, Department of Neuroscience, Yamaguchi University School of Medicine, 1-1-1 Minami-Kogushi, Ube, Yamaguchi 755-8505, Japan
Tel: +81 836 22 2204; fax: +81 836 22 2205;
e-mail: shinoda@yamaguchi-u.ac.jp

Received 14 December 2010 **accepted** 24 January 2011

Introduction

The stigmoid body (STB) was first identified as a distinct, spherical-to-ovoidal, nonmembrane-bound inclusion (0.5–3 μm in diameter) in the cytoplasm of neurons in the limbic and the hypothalamus of healthy rats [1–3]. The STB has none of the aggresomal characteristics, such as being ubiquitinated and surrounded by vimentin, indicating that the STB is a physiological entity distinct from pathological aggresome [4]. Huntingtin-associated protein 1 (HAP1) induces the formation of STB by its complementary DNA (cDNA) transfection into HEK293 cells [5] and it is detected in the STB of the rat brain [6]. In the mouse brain, the STB and HAP1 messenger RNA have a similar distribution [7] and the STB formation is suppressed in the brain of *Hap1* (+/−) mice [8]. This evidence has led to the suggestion that HAP1 is an essential component, hence a marker, of STBs [3].

HAP1 interacts with huntingtin in polyglutamine(polyQ)-dependent manner [9] and has a protective effect on neurons against apoptosis induced by polyQ-expanded huntingtin [7,8]. HAP1/STB also interacts with polyQ-expanded androgen receptor (AR) in polyQ-dependent manner through a ligand-binding domain, and it suppresses apoptosis induced by a polyQ-expanded AR derived from spinal and bulbar muscular atrophy (SBMA) [10]. In addition, HAP1/STB is associated with TATA-binding protein [11], the polyQ-expansion of which causes spinocerebellar ataxia type 17 (SCA17), and Abelson helper integration site 1 [12], mutations of which are linked to nontriplet neuropsychiatric diseases including Joubert syndrome and schizophrenia [13]. The line of data suggests that HAP1/STB could play a protective role in Huntington's disease, SBMA, SCA17, and Joubert syndrome, leading to the 'HAP1/STB protection hypothesis' that HAP1/STB expression raises the threshold of vulnerability for neurodegeneration and renders more beneficial stability to neurons with HAP1/STB than without it [7]. It remains to be determined, however, how far the hypothesis can be applied to other neural disorders.

In this study, to screen what other neural-disorder-related molecules are possibly involved in the interaction with HAP1/STBs, we cloned causative molecules in several representative neural disorders from normal human brain RNA library and evaluated their subcellular interaction with HAP1/STB in Neuro2a cells.

Methods

Plasmids and Cell culture

Plasmids used here were PCR-amplified using the primers listed in Supplementary Table 1 (Supplemental digital content 1 *http://links.lww.com/WNR/A106*). As target molecules, we choose amyloid precursor protein (APP) in Alzheimer-type dementia, α-synuclein, ubiquitin carboxy-terminal esterase L1 (UCH-L1) in Parkinson's disease, transactive

Supplemental digital content is available for this article. Direct URL citations appear in the printed text and are provided in the HTML and PDF versions of this article on the journal's Website (*www.neuroreport.com*).

DOI: 10.1097/WNR.0b013e32834505f4

response DNA-binding protein of 43 kDa (TDP-43) in amyotrophic lateral sclerosis, ataxin-1 in SCA1, ataxin-3 in SCA3, and monoamine oxidase A (MAO-A) in schizophrenia. HAP1 cDNA obtained from Full-length Human Clone Collection (Invitrogen, Carlsbad, California, USA) were cloned into the *Eco*RI-*Xho*I-digested pcDNA3 vector (Invitrogen). The isolation of ataxin-3Q27 and ataxin-3Q79 cDNAs has been described earlier [14] and was used to reconstruct FLAG-tagged ataxin-3Q27 and ataxin-3Q79 using Gateway technology (Clontech, Mountain View, California, USA). Ataxin-3 deletion mutants were amplified from cDNA encoding ataxin-3 by PCR. The cDNAs of the other target molecules were obtained from human brain total RNA (Clontech) by reverse transcriptase-PCR and were used to construct p3 × FLAG-CMV-10 vector (SIGMA, St Louis, Missouri, USA) using Gateway technology. The plasmids cloned in this study were verified by sequencing. The mouse neuroblastoma (Neuro2a) cell culture was done as described earlier [10].

Western blot analysis, fluorescence immunocytochemistry, cell count, and statistical analysis

Western blot analysis and immunocytochemistry with rabbit anti-HAP1 polyclonal antibody (HAP1 H-300, Santa Cruz Biotechnology, Santa Cruz, California, USA) and mouse anti-FLAG monoclonal antibody (FLAG-M5, Sigma-Aldrich, Tokyo, Japan) was performed as described earlier [3,10]. Image analysis, cell count, and statistical analysis was performed as described earlier [10].

Immunoprecipitation and quantitative analysis

Immunoprecipitation was performed using the FLAG Immunoprecipitation kit (Sigma-Aldrich) according to the manufacturer's instructions. Quantitative analysis was performed as described earlier [10].

Results

The expression vectors of HAP1 and FLAG-tagged ataxin-1, ataxin-3Q27, α-synuclein, UCH-L1, APP, TDP-43, and MAO-A were constructed and singly transfected. Western blot analysis of these transfected cell lysates showed distinct bands corresponding to their expected molecular weights (Fig. 1a and b). Most of the cultured cells transfected with HAP1 were observed to form HAP1-immunoreactive solitary inclusions in cytoplasm (HAP1/STBs) as reported earlier [4,5,7] (see Figure 1a Supplemental digital content 2 *http://links.lww.com/WNR/A107*). Immunofluorescence cytochemistry showed that ataxin-1 or TDP-43 was localized mainly in the nucleus (see Figures 1b and f Supplemental digital content 2 *http://links.lww.com/WNR/A107*), whereas ataxin-3Q27, APP, or MAO-A was expressed mainly in the cytoplasm (Fig. 1c, see Figures 1e and g Supplemental digital content 2 *http://links.lww.com/WNR/A107*). UCH-L1 and α-synuclein showed diffused expression in both nucleus and cytoplasm (see Figures 1c and d Supplemental digital content 2 *http://links.lww.com/WNR/A107*).

To evaluate the intracellular relationship between HAP1 and the abovementioned target molecules, the expression vectors of HAP1 and each causative molecule were cotransfected. Cotransfection of expression vectors of HAP1 and ataxin-3Q27 induced distinct cytoplasmic aggregations that were HAP1/ataxin-3 double positive (Fig. 1g–i). In contrast, the other molecules did not interact with HAP1-immunoreactive inclusions (Fig. 1d–f and j–x) and their intracellular localizations in single transfection were unchanged even after cotransfection with HAP1/STB.

To determine the region of ataxin-3 crucial for interaction with HAP1, the expression vectors of three kinds of ataxin-3-deletion mutants were created (Fig. 2a). They included cDNAs encoding Josephin domain (ATX3 1-510), ataxin-3 lacking Josephin domain (ATX3Q27 511-1083), and ataxin-3 lacking Josephin domain and ubiquitin-interacting motifs (ATX3Q27 781-1083). In western blots, cell lysates from the transfected cells showed the expected molecular weights of all these mutants (Fig. 2b). Immunofluorescence cytochemistry showed that a single transfection of ATX3Q27 511-1083 or ATX3Q27 781-1083 resulted in entirely diffused expression (Fig. 2c and d), whereas ATX3 1-510 was expressed ambiguously in nucleus and part of the cytoplasm (Fig. 2e).

Cotransfections of the expression vectors of ATX3 1-510 and HAP1 induced the formation of prominent HAP1/ATX3 1-510 double-labeled cytoplasmic aggregations (Fig. 2l–n). In contrast, cotransfection of HAP1 and ATX3Q27 511-1083 or 781-1083 did not result in HAP1 double-labeled cytoplasmic aggregations (Fig. 2f–k). Then, the coimmunoprecipitation experiment was carried out to biochemically investigate the interaction of the HAP1/STB and ataxin-3Q27 or Josephin domain (Fig. 2o and p). In cells coexpressing HAP1 and ataxin-3Q27 or ATX3 1-510, HAP1 coprecipitated with ataxin-3Q27 and ATX3 1-510. However, HAP1 did not coprecipitate with ATX3Q27 511-1083. The results clearly show that the Josephin domain itself is an essential region for association with HAP1/STB.

A FLAG-tagged-ataxin-3 (ataxin-3Q79) was created (Fig. 3a). In western blots, cell lysates from the transfected cells showed the expected molecular weights (Fig. 3b). Most of the cells were observed to express ataxin-3Q79 diffusely in the nuclei and cytoplasm in fluorescence microscopy (Fig. 3c). Immunofluorescence cytochemistry showed that the HAP1/ataxin-3 double-labeled cytoplasmic-aggregation (Fig. 3d–f). To clarify the difference in the frequency or strength of association with HAP1 between ataxin-3Q27 and ataxin-3Q79, the HAP1/ataxin-3 double-labeled cytoplasmic aggregation formation (HA3-CAF) ratios (HA3-CAF cell number/total cotransfected cell

Fig. 1

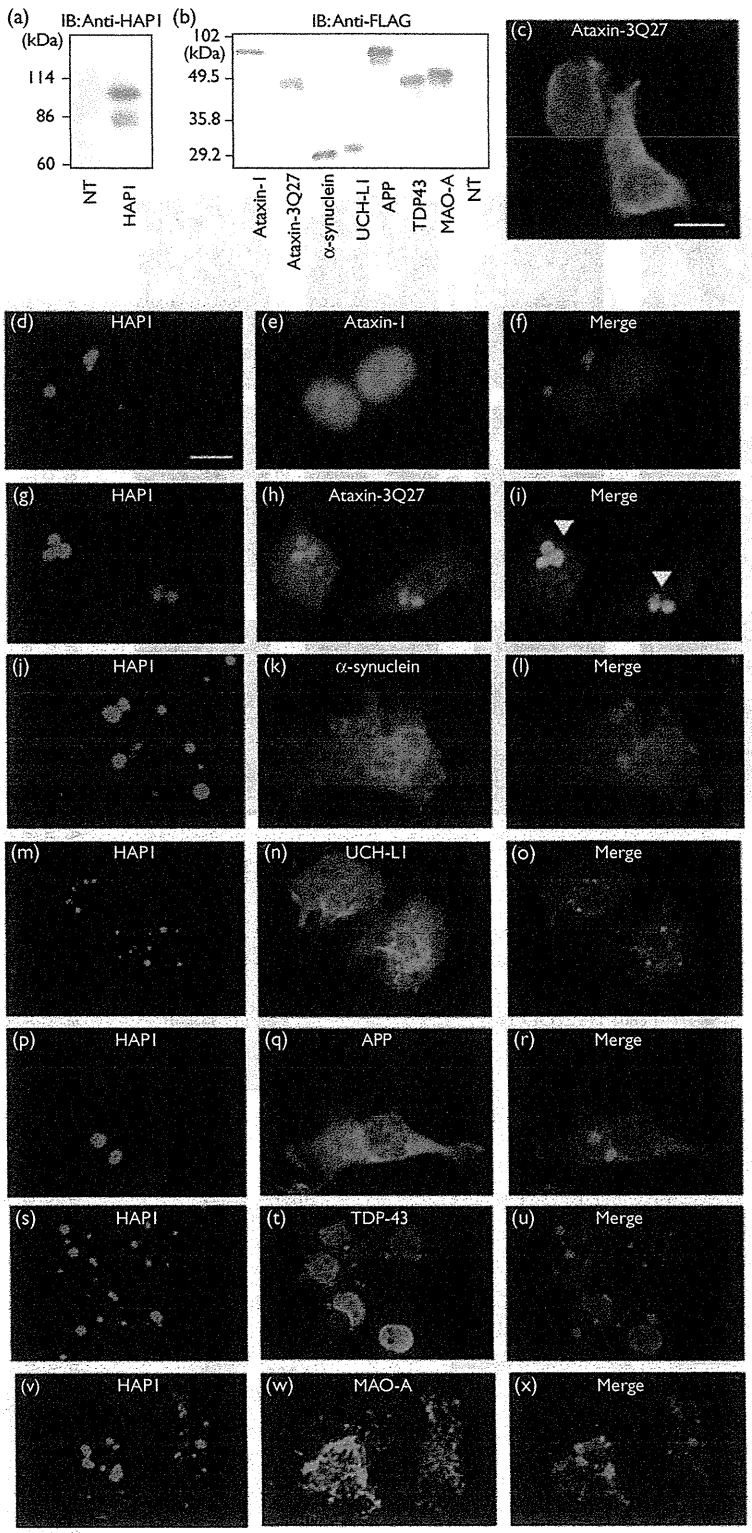

Cotransfection of huntingtin-associated protein 1 (HAP1) and target molecules. (a and b) Western blots for nontransfected (NT) cells and cells transfected with HAP1 (a) and FLAG-tagged target molecules including ataxin-1, ataxin-3Q27, α-synuclein, ubiquitin carboxy-terminal esterase L1 (UCH-L1), amyloid precursor protein (APP), transactive response DNA-binding protein of 43 kDa (TDP-43), and monoamine oxidase A (MAO-A) (b). Molecular weights (kDa) are indicated on the left side. (c) Fluorescence immunocytochemistry for ataxin-3Q27-transfected cells. (d–x) Fluorescence microscopic images of cells cotransfected with HAP1 (Alexa488: green) and target molecules (Alexa594: red). Arrowheads indicate ataxin-3Q27 was associated with HAP1/stigmoid body (f) (bar=10 μm).

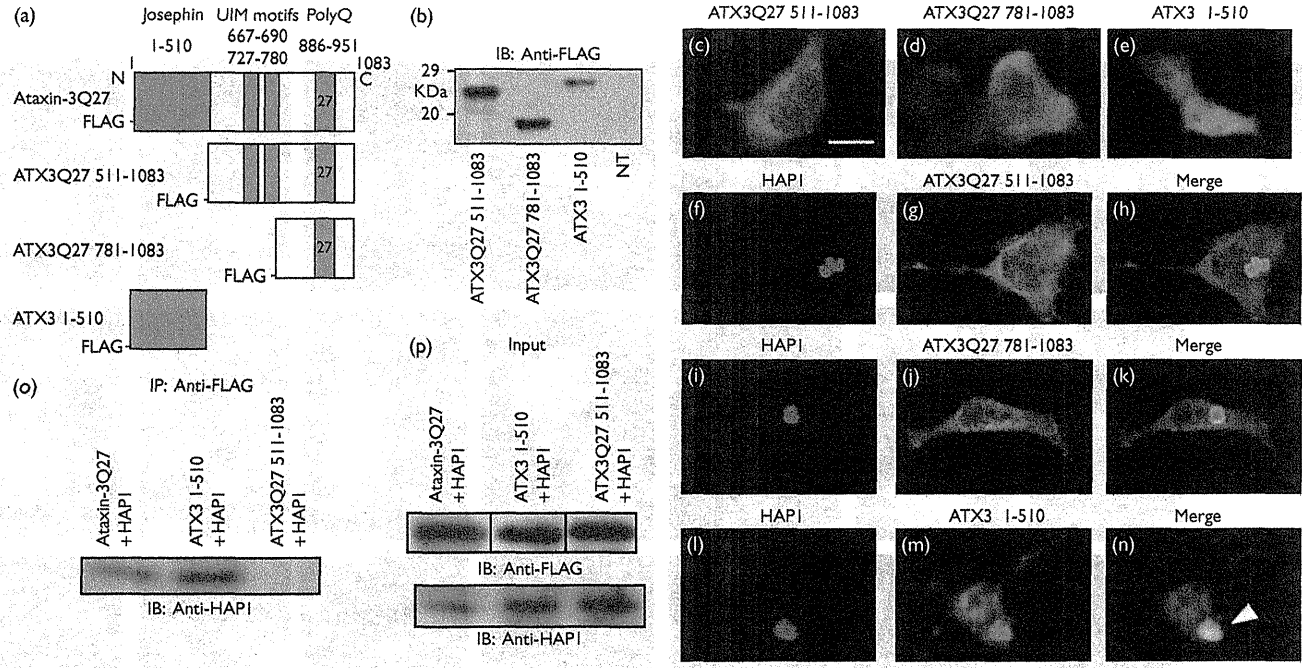

Construction of ataxin-3-deletion mutants and cotransfection of huntingtin-associated protein 1 (HAP1) and these mutants. (a) Schematic representation of ataxin-3Q27 and ataxin-3-deletion mutants. Each mutant is FLAG-tagged in the *N*-terminus. ATX3Q27 511-1083, ataxin-3-lacking Josephin domain; ATX3Q27 781-1083, ataxin-3-lacking Josephin domain and ubiquitin-interacting motifs; and ATX3 1-510, Josephin domain. (b) Western blot analysis for the lysates from cells transfected with each ataxin-3-deletion mutants. (c–e) Fluorescence microscopic images of Neuro2a cells transfected with three ataxin-3-deletion mutants. (f–n) Fluorescence photomicrographs showing subcellular interactions between HAP1 and three ataxin-3-deletion mutants. Arrowhead indicates that ATX3 1-510 is associated with HAP1/stigmoid body (n). (o and p) Coimmunoprecipitation of HAP1 with ataxin-3Q27, ATX3Q27 1-510, or ATX3Q27 511-1083. Cell lysates were prepared and subjected to immunoprecipitation with anti-FLAG M2 affinity gel. Immunoprecipitated samples are analyzed by western blotting using the anti-HAP1 antibody. Inputs are the control of proteins exogenously expressed (bar = 10 μm).

number) were surrogated as an index and chronologically compared between HAP1/ataxin-3Q27 and HAP1/ataxin-3Q79-cotransfected cells. The HA3-CAF ratios for ataxin-3Q27 and ataxin-3Q79 (HA3Q27-CAF and HA3Q79-CAF ratios) were approximately 33.7 and 34.8% in 24 h and 34.1 and 36.1% in 48 h after each cotransfection (Fig. 3g). There was no significant difference between HA3Q27-CAF and HA3Q79-CAF ratios. Coimmunoprecipitation tests were carried out to obtain biochemical evidence for the interaction of HAP1 with ataxin-3Q27 or ataxin-3Q79 (Fig. 3h–j).

Fig. 3

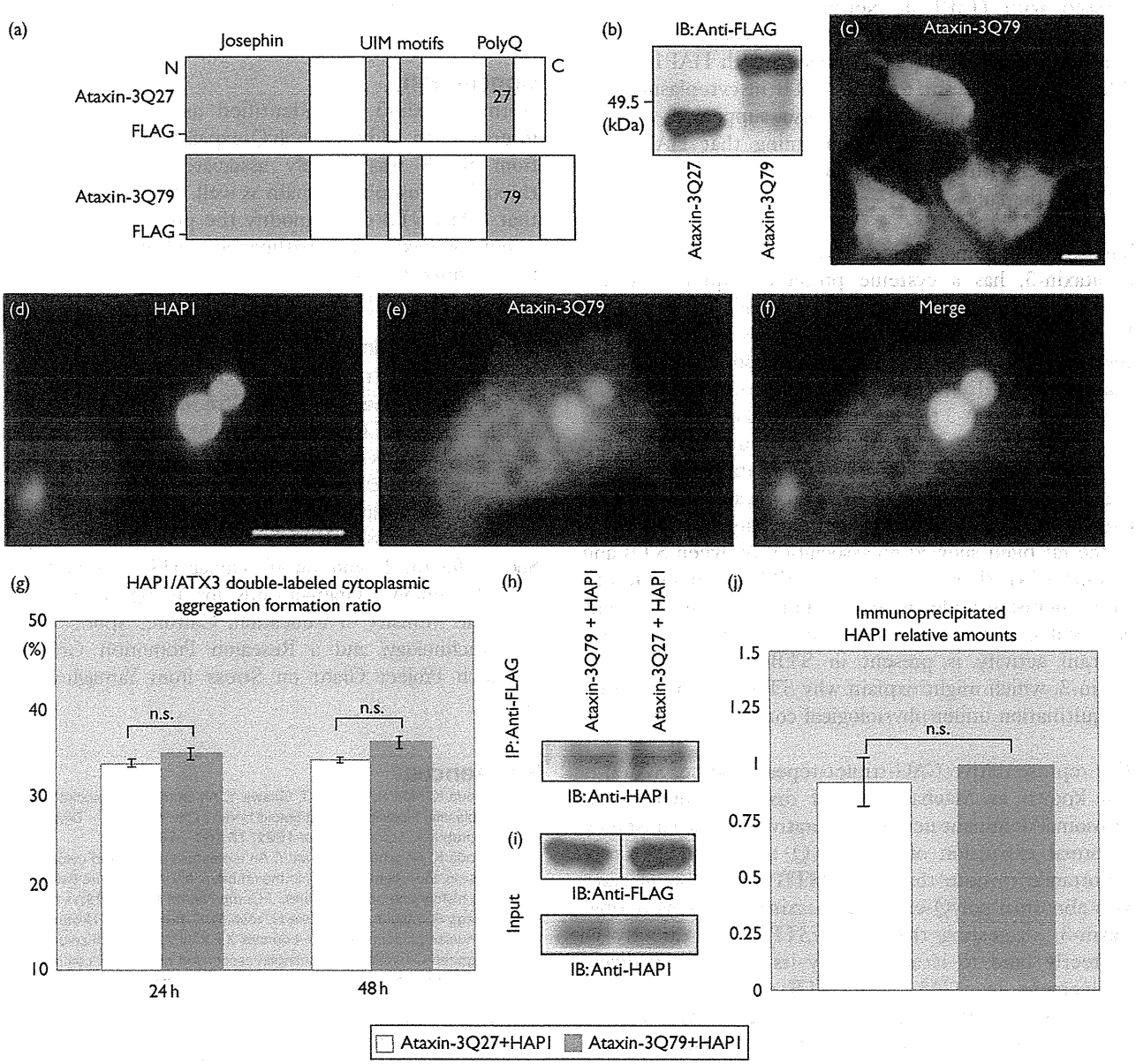

Interaction of huntingtin-associated protein 1 (HAP1)/stigmoid body with polyQ-expanded ataxin-3. (a) Diagrams of the primary structures of ataxin-3Q27 and ataxin-3Q79. (b) Western blot for extracts from ataxin-3Q27-transfected and ataxin-3Q79-transfected cells. (c) Fluorescence immunocytochemistry for ataxin-3Q79-transfected cells. (d–f) Fluorescence photomicrographs showing subcellular expression of HAP1 and ataxin-3Q79. Note that merged images show colocalization of HAP1 and ataxin-3Q79 (f) (bars=10 μm). (g) Bar graph comparing HAP1/ataxin-3 double-labeled cytoplasmic aggregation formation ratios between ataxin-3Q27 and ataxin-3Q79 in time course (24 and 48 h) after the cotransfection into cells (ns, not significant). (h and i) Coimmunoprecipitation analysis of protein lysates from HAP1/ataxin-3Q27-cotransfected and HAP1/ataxin-3Q79-cotransfected cells. Inputs are the control of proteins exogenously expressed. (j) Quantification of the each immunoprecipitated HAP1 protein normalized to ataxin-3Q27 and ataxin-3Q79.

In cells coexpressing HAP1 and ataxin-3Q27, or ataxin-3Q79, HAP1 was coprecipitated. There was no significant difference in immunoprecipitated HAP1 relative amounts between ataxin-3Q27 and ataxin-3Q79.

Discussion

In this study, the most striking finding is that HAP1/STB are closely associated with normal ataxin-3Q27 and mutant ataxin-3Q79 derived from a SCA3 patient. Furthermore, even the Josephin domain alone coexpressed with HAP1 in Neuro2a cells clearly showed intimate association with HAP1/STB, whereas Josephin-deleted mutant ataxin-3 coexpressed with HAP1 turned diffuse and irrelevant to HAP1/STB in cytoplasm. Data for immunoprecipitation assay also supported the immunocytochemical results, confirming that HAP1/STB can interact with normal and mutant ataxin-3 through its Josephin domain.

The Josephin domain, which is located at the *N*-terminus of ataxin-3, has a cysteine protease sequence, which suggests potential ubiquitin protease activity [15]. Josephin domain also represses histone acetylation and transcription by binding to histone and transcriptional coactivator [16]. As HAP1/STB is intracellularly associated with ataxin-3 through its Josephin domain, it might partially modify the function of the putative ubiquitin protease or transcriptional repressor of ataxin-3. Interestingly, ataxin-3 was reported to be a typical deubiquitinating enzyme [17]. Our earlier immunohistochemical study in the rat brain showed no association between STB and ubiquitin [4], showing that HAP1/STB is a nonubiquitinated inclusion under normal conditions. Thus, it might be possible that a deubiquitinating enzyme or deubiquitination activity is present in STBs with HAP1 and ataxin-3, which might explain why STBs are spared from ubiquitination under physiological conditions.

The representative CAG-triplet-repeat disease, SCA3, is also known as Machado–Joseph disease, which is an autosomal dominant neurodegenerative disease caused by abnormal expansion of the polyQ tract [14]. It is of importance to note that HAP1/STB could also interact with abnormal polyQ-expanded ataxin3 as well as normal ataxin-3, suggesting that HAP1/STB could directly or indirectly bind to it and modify its pathophysiological involvement in SCA3. HAP1/STB also interacts with polyQ-expanded huntingtin and AR and suppresses their nuclear translocation in polyQ-dependent manner [9,10]. Thus, it could more efficiently neutralize the toxicity of the polyQ-expanded mutant forms in pathogenesis of Huntington's disease and SBMA and protect against the cell death. In SCA17 and Joubert syndrome, the affinities of HAP1/STB with pathological mutants of TATA-binding protein and Abelson helper integration site 1 are less strong than normal forms [11,12]. Nevertheless, HAP1/STB could serve as a cytoplasmic neuroprotective component interfering with 'gain-of-toxic function' of their pathological mutants [11,12]. HAP1/STB expression might raise the threshold of vulnerability for cell death and render more beneficial stability to cells with HAP1/STB than without it, as the 'HAP1/STB protection hypothesis' predicts [7]. Thus, in this study, although HAP1/STB seems to interact with ataxin-3 in polyQ-independent manner, it might be possible that HAP1/STB plays an important role in modification on physiological functions of normal ataxin-3 and on SCA3 pathogenesis attributable to ataxin-3Q79.

Conclusion

Normal ataxin-3 was identified as a new HAP1/STB interactor. In addition, polyQ-expanded ataxin-3 derived from SCA3 was closely associated with HAP1/STB through its Josephin domain as well. The findings suggest that HAP1/STB could modify the physiological function of normal ataxin-3 and pathogenesis of SCA3 attributable to the mutant ataxin-3.

Acknowledgements

We are grateful to Ms. Yurika Koto, Ms. Risa Andachi, Mr. Chikahisa Matsuo, Mr. Jun Oba, Ms. Yumiko Matsuzaki, and Ms. Miyuki Takeshita for technical assistance in the early stages of this study. We also acknowledge the technical expertise of the DNA Core facility of the Center for Gene Research, Yamaguchi University. This study was supported by Grant-in-Aid for Scientific Research (C) from the Japan Society for the Promotion of Science (JSPS), Grant-in-Aid for JSPS fellows, Grant-in-Aids for Young Scientists (B) from the Ministry of Education, Culture, Sports, Science and Technology, and a Research Promotion Grant and Research Project Grant on Stress from Yamaguchi University.

References

1 Shinoda K, Mori S, Ohtsuki T, Osawa Y. An aromatase-associated cytoplasmic inclusion, the 'stigmoid body,' in the rat brain: I. Distribution in the forebrain. *J Comp Neurol* 1992; **15**:360–376.
2 Shinoda K, Nagano M, Osawa Y. An aromatase-associated cytoplasmic inclusion, the 'stigmoid body,' in the rat brain: II. Ultrastructure (with a review of its history and nomenclature). *J Comp Neurol* 1992; **329**:1–19.
3 Fujinaga R, Yanai A, Nakatsuka H, Yoshida K, Takeshita Y, Uozumi K, *et al.* Anti-human placental antigen complex X-P2 (hPAX-P2) anti-serum recognizes C-terminus of huntingtin-associated protein 1A common to 1B as a determinant marker for the stigmoid body. *Histochem Cell Biol* 2007; **128**:335–348.
4 Fujinaga R, Takeshita Y, Uozuimi K, Yanai A, Yoshioka K, Kokubu K, *et al.* Microtubule-dependent formation of the stigmoid body as a cytoplasmic inclusion distinct from pathological aggresomes. *Histochem Cell Biol* 2009; **132**:305–318.
5 Li SH, Gutekunst CA, Hersch SM, Li XJ. Association of HAP1 isoforms with a unique cytoplasmic structure. *J Neurochem* 1998; **71**:2178–2185.
6 Gutekunst CA, Li SH, Yi H, Ferrante RJ, Li XJ, Hersch SM. The cellular and subcellular localization of huntingtin-associated protein 1 (HAP1): comparison with huntingtin in rat and human. *J Neurosci* 1998; **18**:7674–7686.
7 Fujinaga R, Kawano J, Matsuzaki Y, Kamei K, Yanai A, Sheng Z, *et al.* Neuroanatomical distribution of huntingtin-associated protein 1-mRNA in the male mouse brain. *J Comp Neurol* 2004; **478**:88–109.

8 Li SH, Yu ZX, Li CL, Nguyen HP, Zhou XY, Deng C, *et al.* Lack of huntingtin-associated protein-1 causes neuronal death resembling hypothalamic degeneration in Huntington's disease. *J Neurosci* 2003; **23**:6956–6964.

9 Li XJ, Li SH, Sharp AH, Nucifora FC Jr, Schilling G, Lanahan A, *et al.* A huntingtin-associated protein enriched in brain with implications for pathology. *Nature* 1995; **378**:398–402.

10 Takeshita Y, Fujinaga R, Zhao C, Yanai A, Shinoda K. Huntingtin-associated protein 1 (HAP1) interacts with androgen receptor (AR) and suppresses SBMA-mutant-AR-induced apoptosis. *Hum Mol Genet* 2006; **15**:2298–2312.

11 Prigge JR, Schmidt EE. HAP1 can sequester a subset of TBP in cytoplasmic inclusions via specific interaction with the conserved TBP(CORE). *BMC Mol Biol* 2007; **8**:76.

12 Sheng G, Xu X, Lin FY, Wang CE, Rong J, Cheng D, *et al.* Huntingtin-associated protein 1 interacts with Ahi1 to regulate cerebellar and brainstem development in mice. *J Clin Invest* 2008; **118**:2785–2795.

13 Tori F, Akelai A, Lupoli S, Siromi M, Amann-Zaicenstein D, Fumagalli MA, *et al.* Fine mapping of AHI1 as a schizophrenia susceptibility gene: from association to evolutionary evidence. *FASEB J* 2010; **24**: 3066–3082.

14 Kawaguchi Y, Okamoto T, Taniwaki M, Aizawa M, Inoue M, Katayama S, *et al.* CAG expansions in a novel gene for Machado-Joseph disease at chromosome 14q32.1. *Nat Genet* 1994; **8**:221–228.

15 Doss-Pepe EW, Stenroos ES, Johnson WG, Madura K. Ataxin-3 interactions with Rad3 and valosin-containing protein and its associations with ubiquitin chains and the proteasome are consistent with a role in ubiquitin-mediated proteolysis. *Mol Cell Biol* 2003; **23**:6469–6483.

16 Li F, MacFarlan T, Pittman RN, Chakravarti D. Ataxin-3 is a histone-binding protein with two independent transcriptional corepressor. *J Biol Chem* 2002; **277**:45004–45012.

17 Burnett B, Li F, Pittman RN. The polyglutamine neurodegenerative protein ataxin-3 binds polyubiquitylated proteins and has ubiquitin protease activity. *Hum Mol Genet* 2003; **12**:3195–3205.

Longitudinal and Simultaneous Imaging of Retinal Ganglion Cells and Inner Retinal Layers in a Mouse Model of Glaucoma Induced by *N*-Methyl-D-Aspartate

Noriko Nakano,[1] *Hanako Ohashi Ikeda,*[1] *Masanori Hangai,*[1] *Yuki Muraoka,*[1] *Yoshinobu Toda,*[2] *Akira Kakizuka,*[3] *and Nagahisa Yoshimura*[1]

Purpose. To investigate the longitudinal profile of *N*-methyl-D-aspartate (NMDA) injection-induced damage in retinal ganglion cells (RGCs) by imaging retinal Thy 1-cyan fluorescent protein (CFP) expression and inner retinal layers using a custom-made imaging device containing short-wavelength confocal scanning laser ophthalmoscope (scSLO) and speckle noise-reduced spectral-domain optical coherence tomography (SD-OCT).

Methods. Simultaneous scSLO and SD-OCT examinations were performed in Thy 1-CFP mice injected with NMDA (1–20 nanomoles). CFP-expressing RGCs were counted using scSLO images. Ganglion cell complex (GCC: retinal nerve fiber layer, ganglion cell layer, and inner plexiform layer) thickness around the optic disc was measured in SD-OCT images.

Results. The RGCs rapidly decreased 1 day after NMDA injection in a dose-dependent manner (65.3%, 71.7%, 49.5%, and 27.1% of the preinjection level, 2, 5, 10, and 20 nanomoles, respectively) and continued to decrease slightly (to 53.7%, 44.1%, 28.3%, and 20.2% of the preinjection level on days 14, 2, 5, 10, and 20 nanomoles, respectively). In contrast, dose-dependent reduction of GCC thickness was first detected 4 days after injection. The thickness further decreased to 84.6%, 75.7%, 76.5%, and 71.4% of the preinjection level on day 14 (2, 5, 10, and 20 nanomoles, respectively).

Conclusions. NMDA-induced RGC damage is characterized by rapid RGCs loss followed by gradual reduction in GCC thickness. Simultaneous imaging of CFP expression in the RGCs and inner retinal layers provides a sensitive, reliable, and new method for longitudinal evaluation of progressive RGC damage in experimental models of glaucoma. (*Invest Ophthalmol Vis Sci.* 2011;52:8754–8762) DOI:10.1167/iovs.10-6654

Glaucoma, the second leading cause of vision loss in the world,[1] is caused by progressive retinal ganglion cell (RGC) loss due to damage to the RGC axon within the optic nerve head[2] and damage to the soma of the RGC. Currently, several noninvasive methods for in vivo experimental assessment of progressive RGC loss have been performed, using high-end optical imaging technologies including optical coherence tomography (OCT) and confocal scanning laser ophthalmoscopy (cSLO), which provide a unique opportunity to study RGC injury longitudinally without euthanizing animals at multiple time points.[3–12]

OCT is an interferometric imaging technology and enables high-resolution, cross-sectional imaging of fundus structures in vivo. It has been clinically used in glaucoma patients to help diagnosis of the disease or to monitor disease progression. For example, circumpapillary retinal nerve fiber layer (cpRNFL) thickness or macular ganglion cell complex (GCC) thickness, which includes the RNFL, ganglion cell layer (GCL), and inner plexiform layer (IPL) has been shown to be useful and reliable to diagnose or to assess the disease. In experimental glaucoma models, OCT also allows investigators to monitor changes in the thickness of the whole retina and the retinal nerve fiber layer (RNFL) in rodents.[5,10–12] In contrast with originally developed time-domain OCT (TD-OCT), recently developed spectral-domain OCT (SD-OCT) technology improves visualization of the individual retinal layers, such as GCL and IPL, by speckle noise reduction, which is the most influential artificial noise that blurs the boundaries of the retinal layers.[13] Especially, SD-OCT with a three-dimensional eye-tracking system enables obtaining multiple B-scans at an identical location of interest. Exact averaging of B-scans results in a sufficient reduction in speckle noise to greatly improve visualization of RGC-related inner retinal layer boundaries.[12,14] The technique would enable more reliable assessment of the decreasing thickness of the individual inner retinal layers and RGC-related complex as RGC injuries progress in glaucoma patients[15–18] and in rodents models of glaucoma.[12]

On the other hand, cSLO enables investigators to directly monitor individual RGCs that are labeled genetically[6,7,9] or by retrograde labeling[4] and apoptotic RGCs that are labeled fluorescently with annexin 5 (DARC).[3] Because RGC imaging at the cellular level is not feasible in living human eyes, the RGC imaging methods using cSLO in experimental animals provide unique advantages for investigating the pathogenesis of RGC death. Moreover, counting the number of RGCs on cSLO images of identical eyes at multiple time points facilitates assessment of the neuroprotective effects of drugs or chemicals on RGCs in vivo. The thickness of the inner retinal layer and the number of RGCs are associated with RGC damage in the same

From the [1]Department of Ophthalmology and Visual Sciences and the [2]Center for Anatomical Studies, Kyoto University Graduate School of Medicine, Kyoto, Japan; and the [3]Laboratory of Functional Biology, Kyoto University Graduate School of Biostudies and Solution Oriented Research for Science and Technology, Kyoto, Japan.

Presented at the annual meeting of the Association for Research in Vision and Ophthalmology, Fort Lauderdale, Florida, May 2010.

Supported in part by the Innovative Techno-Hub for Integrated Medical Bio-imaging Project of the Special Coordination Funds for Promoting Science and Technology; Grant-in-Aid for Young Scientists 22791656 from the Ministry of Education, Culture, Sports, Science and Technology (MEXT); and a research grant from the Astellas Foundation for Research on Metabolic Disorders.

Submitted for publication September 29, 2010; revised January 31, May 31, and September 1, 2011; accepted October 9, 2011.

Disclosure: **N. Nakano**, None; **H.O. Ikeda**, None; **M. Hangai**, None; **Y. Muraoka**, None; **Y. Toda**, None; **A. Kakizuka**, None; **N. Yoshimura**, None

Corresponding author: Hanako Ohashi Ikeda, Department of Ophthalmology and Visual Sciences, Kyoto University Graduate School of Medicine, 54 Kawahara-cho, Shogoin, Sakyo-ku, Kyoto 606-8507, Japan; hanakoi@kuhp.kyoto-u.ac.jp.

Investigative Ophthalmology & Visual Science, November 2011, Vol. 52, No. 12

experimental setting using identical animals. However, no previous studies have monitored these two distinct but mutually related parameters simultaneously.

To reveal the relationship between RGC damage at the cellular level and retinal thickness related to the RGCs, we developed a custom-made imaging system for animals based on a commercial system (Spectralis HRA+OCT; Heidelberg Engineering, Heidelberg, Germany). The combined system contains a cSLO, a custom-made short-wavelength confocal scanning laser ophthalmoscope (scSLO), and an SD-OCT system with an eye-tracking function. In addition to a laser for detecting fluorescein protein (488 nm), the instrument includes a laser with a short wavelength (445 nm) that is optimized for detecting cyan fluorescent protein (CFP; major excitation peak, 433 nm; major emission peak, 475 nm).[19] This approach enables detection of individual RGCs in Thy 1-CFP transgenic mice,[20] in which CFP expression is controlled by the *Thy 1* promoter. Thy 1 is a cell-surface glycoprotein expressed by projection neurons in many parts of the nervous system[21]; in the retina, it is most exclusively expressed in RGCs.[22]

N-methyl-D-aspartate (NMDA)-induced excitotoxicity is a well-known model to induce RGC injury.[23] In the retina, RGCs and a subset of cells in the inner nuclear layer (INL) express subunits of NMDA receptor. RGCs are exquisitely sensitive to the effects of glutamate and the glutamate analog NMDA, which causes dose-dependent loss of RGCs.[23,24] NMDA-induced excitotoxicity, as well as neurotrophin deprivation induced by optic nerve crush or transection, has been implicated in the pathogenesis of glaucoma and widely used as a glaucoma model.[25,26]

The purpose of this study was to determine the feasibility of longitudinal monitoring of RGC damage, on both individual cell imaging and measurement of the thickness of inner retinal layers using combined scSLO and speckle noise-reduced SD-OCT. Using intravitreal NMDA injection to induce RGC injury, we assessed the profile of progressive RGC degeneration from the dual aspects of the number of CFP-expressing RGCs and the thickness of the ganglion cell complex (GCC), which includes RNFL, RGC, and IPL in Thy 1-CFP transgenic mice.

Methods

Combined Imaging System of scSLO and Speckle Noise–Reduced SD-OCT with an Eye-Tracking Function

An imaging system that combines scSLO and speckle noise-reduced SD-OCT with an eye-tracking function was customized (based on a Spectralis HRA+OCT), to modify the SLO system to an optimal wavelength of light source for CFP imaging (termed the Multiline OCT system) by Heidelberg Engineering (Heidelberg, Germany). This system includes a short-wavelength (445 nm) diode laser and a barrier filter with a 488-nm cutoff to visualize the CFP protein. The scan rate of the scSLO is 12 frames per second, with a digital resolution of 512 × 512 pixels in each frame. The OCT instrument uses an 870-nm superluminescent diode as a light source. The scan rate of the SD-OCT is 47,000 A-scans per second, with an axial resolution of ~7 μm. The simultaneous SLO and SD-OCT imaging of the retina enables real-time three-dimensional tracking of eye movements, which allows precise real-time averaging of multiple SLO and B-scan images acquired at each identical location of interest on the retina to reduce speckle noise.[14]

Experimental Animals

All studies were conducted in compliance with the ARVO Statement for the Use of Animals in Ophthalmic and Vision Research. Transgenic mice, B6.Cg-Tg (Thy 1-CFP) 23Jrs/J, in which CFP is expressed under the *Thy 1* promoter were obtained from the Jackson Laboratory (Bar Harbor, ME). Genotyping was performed with the PCR method, as instructed. The environment was maintained in 12-hour light–dark cycle. All the mice were fed ad libitum. Male mice (age, 8–10 weeks; weight, 25–30 g) were used in the experiments. Before image acquisition or intravitreal injection, the mice were anesthetized by an intraperitoneal injection of pentobarbital (50 mg/kg body weight). Pupils were dilated to approximately 2 mm in diameter with tropicamide and phenylephrine (0.5% each) eye drops.

Mouse Acute RGC Injury Model Mediated by NMDA

NMDA (20 nanomoles/2 μL [n = 15], 10 nanomoles/2 μL [n = 15], 5 nanomoles/2 μL [n = 10], 2 nanomoles/2 μL [n = 10], and 1 nanomoles/2 μL [n = 6]) was injected into the vitreous of the eyes of Thy 1-CFP mice using a 33-gauge needle (Ito Corporation, Shizuoka, Japan). Control mice (n = 15) were injected with the same volume of phosphate-buffered saline (PBS).

Image Acquisition

scSLO and SD-OCT examinations were performed simultaneously at 1, 2, 4, 7, and 14 days after the injection. For fundus imaging, PMMA contact lenses optimal for mice (Heidelberg Engineering) were placed on the corneas. Use of the lenses prevents anesthesia-induced cataract progression. A 25-D adaptor lens was placed on the objective lens of the Multiline OCT to focus on the mouse retina. For imaging of the inner retinal layers on SD-OCT using the speckle noise-reduction method, six radial B-scans through the optic disc and a circular scan around the optic disc were performed. In this study, the maximum number of B-scans set by the manufacturer (100 for line scans and 16 for circular scans) were used for averaging. For RGC imaging on scSLO, we averaged 30 scSLO images per scan area.

Manual Measurement of GCC Thickness

The software used for drawing boundary lines was based on the built-in Spectralis HRA+OCT and provided by Heidelberg Engineering software to facilitate manual assessment of the B-scan images. This custom-made software allows various boundary lines to be drawn in each B-scan image. The software calculates the distance between the two manually drawn boundary lines for each layer of interest to yield a thickness value at each location. A boundary line was automatically placed along the border of the internal limiting membrane (ILM) and the vitreous, and another boundary line was manually placed between the inner plexiform layer (IPL) and INL in a masked fashion. The distance of these two lines was calculated as the GCC thickness.

With the optimal PMMA contact lens placed on the mouse cornea, the total focal length was 2.00 mm (in air). All lateral dimensions shown by the system software were originally scaled for a human eye, with a focal length of 16.447 mm (in air). This value was obtained using a modified Gullstrand eye and a gradient index lens provided by Heidelberg Engineering (Zinser G, personal communication, 2010). Therefore, to convert the lateral dimensions to those of the mouse eye, we multiplied the values (in millimeters) of the Spectralis by a factor of 2.00/16.447 = 0.122. In mouse eyes, the diameter of the circular scan with 12° (~3.4 mm in human eyes) was calculated as 0.420 mm, and the length of the15° line scan was 0.530 mm.

For GCC measurement along the radial scans, the mean GCC thickness (between 56–224 μm apart from the optic nerve head) along each scan was calculated by the software, and the mean GCC thickness of the six radial scans were averaged. The mean GCC thickness of a circular scan was also calculated by the software.

To assess the intradelineator and interdelineator reliability of the manual measurement of GCC thickness, two delineators (NN and AH) at the Kyoto University OCT Reading Center, who were masked to all experimental information drew the boundary lines for the measurement of GCC thickness on the circular SD-OCT scans. The boundary lines were drawn independently by the two delineators and redrawn on another day by one delineator (AH), as described previously.[27]

Counting of RGC

CFP-positive RGCs were manually counted within four 310-μm squares at a distance of 830 μm from the center of the optic nerve head on the scSLO images in a masked fashion. We selected the best images and determined the best areas in which the cells in the GCL were sharply focused. The number of counted RGCs from the four square areas were averaged.

Histologic Evaluation of Retinas

Immediately after image acquisition, we enucleated the eyeballs from the mice after a pentobarbital overdose. A suture was placed on the edge of the superior conjunctiva to identify the superior portion of the retina. The eyes were fixed in 4% paraformaldehyde for 24 hours at 4°C and embedded in paraffin. Serial 6-μm paraffin-embedded sections were cut through the suture and at the point of insertion of the optic nerve. The sections that passed through the center of the optic nerve head were selected. The selected retinal sections were stained with hematoxylin-eosin and photographed approximately 200 μm apart from the center of the optic disc under an optical microscope (Axioplan 2; Carl Zeiss GmbH, Jena, Germany). For each eye, GCC thickness of each retinal sections at 60, 100, and 200 μm from the optic nerve head (location matched with that at which GCC thickness was measured on radial SD-OCT scans) was measured with image-analysis software (Axio Vision 2.05; Carl Zeiss Vision GmbH), and the values were averaged. In some of these sections, we also counted the number of cells in GCL at days 0 and 1 (for each, $n = 3$).

Immunohistochemical staining was performed with antibodies to green fluorescent protein (GFP; rabbit, 1/500; MBL), syntaxin 1 (HPC-1; mouse, 1/100; Sigma-Aldrich), as a marker for amacrine cells, and Brn3 (goat, 1/50; Santa Cruz Biotechnology, Santa Cruz, CA), for RGC cells.[28] Nuclei were counterstained with a red fluorescent dye (TOTO-3; Invitrogen, Carlsbad, CA). Generally, procedures for fixing the paraffin-embedded sections break the native protein configuration without reducing the protein content, and this weakens the CFP fluorescent signals in the samples. We, therefore, used an anti-GFP antibody to detect the CFP-positive cells during immunohistochemical studies of paraffin-embedded sections. We used frozen sections (20 μm) for the detection of naïve CFP fluorescence and for staining with an anti-GFP antibody, because the fluorescence of CFP was faintly maintained in the frozen sections. The number of cells in the GCL that were positive or negative for each marker in the whole vertical sections (through the optic nerve head) of the retinas collected on days 0, 1, and 14 after NMDA injection (20 nanomoles, $n = 3$) was counted on images acquired with confocal microscopy (LSM 510; Carl Zeiss GmbH).

Statistical Analysis

A paired t-test was used to compare changes in the parameters before and after NMDA injection. Variables among mice injected with different dosage of NMDA were compared by analysis of variance and Scheffé's post hoc test. Linear regression analysis was used to correlate two parameters. The intraclass correlation coefficient (ICC) was calculated to test the intradelineator and interdelineator reliability of the manual measurement of GCC thickness on the circular scans (statistical analyses performed with PASW Statistics ver. 17.0; IBM SPSS, Chicago, IL). The level of statistical significance was set at $P < 0.05$.

Results

Retinal Imaging with Speckle Noise–Reduced SD-OCT Compared with Histologic Tissue Sections in Mice

With speckle noise reduction by averaging multiple B-scans, each layer of the retina, including the RNFL and GCL, in the mice was clearly visualized on the SD-OCT image, although the posterior boundary of the GCL was not as clear as the boundaries of the other layers (Fig. 1A). To test whether we could quantify inner retinal damage on the SD-OCT images, we injected 20 nanomoles of NMDA or PBS as a control into the vitreous of mouse eyes. In the histologic sections, 14 days after the injection, the number of ganglion cells was significantly reduced and the thicknesses of the RNFL, GCL, IPL, and GCC (including the RNFL, GCL, and IPL) were also significantly reduced in the injected eyes compared with the untreated or PBS-injected eyes (Fig. 1B). On the SD-OCT images, location matched with the histologic sections of identical eyes, and the anterior and posterior boundaries of the GCL became less clear

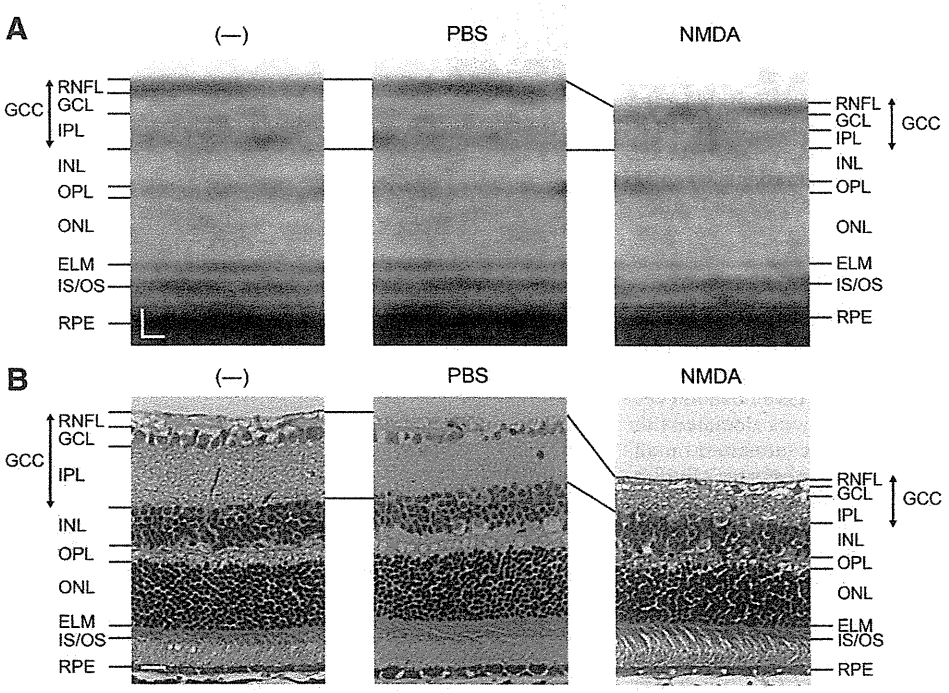

FIGURE 1. (A) Speckle noise–reduced SD-OCT images of mouse retinas. An untreated eye (*left*), an eye injected with PBS (*center*), and an eye injected with NMDA (20 nanomoles, *right*). All the images were location matched, 200 μm superior to the optic nerve head on a vertical scan through the center of the optic nerve head. (B) Retinal sections stained with HE at the retinal location corresponding to the SD-OCT images in (A). RNFL, retinal nerve fiber layer; GCL, ganglion cell layer; IPL, inner plexiform layer; GCC, ganglion cell complex; INL, inner nuclear layer; OPL, outer plexiform layer; ONL, outer nuclear layer; ELM, external limiting membrane; IS/OS, inner and outer segment junction of the photoreceptor cell; and RPE, retinal pigment epithelium. Scale bar, 20 μm.

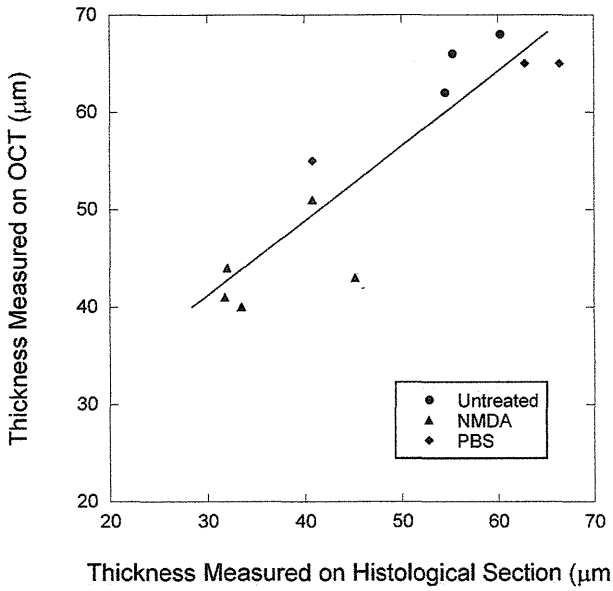

FIGURE 2. The GCC thickness measured on SD-OCT images correlated well with the thickness measured on histologic sections. OCT images (x-axis) versus the location-matched histologic sections (y-axis): r^2 = 0.828, $P < 0.0001$, Pearson's correlation coefficient analysis.

in the NMDA-injected eyes than in the untreated or PBS-injected eyes. However, the boundaries of the GCC (that is, the anterior boundary of the RNFL and the posterior boundary of the IPL) were relatively distinguishable, regardless of the treatment. The SD-OCT images showed that the thickness of the GCC was less in an eye injected with NMDA than in an untreated eye and an eye injected with PBS (Fig. 1A).

To determine whether GCC thickness measured on SD-OCT images correlated with the thickness measured in the histologic sections, it was measured on both the SD-OCT images and the corresponding location-matched histologic sections in the eyes injected with NMDA or PBS, and in untreated eyes. The GCC thickness measured on the SD-OCT images significantly correlated with that measured in the location-matched histologic sections (n = 11, r^2 = 0.828, $P < 0.0001$, Pearson's correlation coefficient analysis; Fig. 2). The mean GCC thickness measured on the SD-OCT images was significantly larger than that measured on the histologic retinal sections (P = 0.027). Thus, the images obtained with speckle noise-reduced SD-OCT were clear enough to distinguish each retinal layer and correlated highly with the histologic sections, both in healthy and damaged mouse retinas.

Correlation between GCC Thickness Measurements on Radial and Circular Scans

To evaluate GCC thickness around the optic disc, we performed six radial scans through the center of the optic nerve head and one circular scan around the optic nerve head in eyes injected with NMDA. Along each radial scan, we calculated the mean GCC thickness and averaged the values measured on all six radial scans. We also calculated GCC thickness on a circular scan image. The mean GCC thickness on the radial scans was compared with that on the circular scan during progressive RGC degeneration. We found a strong association between the GCC thickness measures on radial and circular scans (r^2 = 0.908, $P < 0.001$, Pearson's correlation coefficient analysis; Fig. 3). Taking a measurement on the circular scan image was simpler and faster than taking one on the radial scans; as a result, in the following experiments, we used GCC thickness measured on single circular scan images as the representative GCC thickness in mouse retinas.

Further, we calculated ICCs to assess the intradelineator and interdelineator reliability of the manual measurement of GCC thickness on the circular scans on days 0 and 14 (for each, n = 15). The intradelineator ICCs were 0.842 and 0.971 on day 0, and the interdelineator ICCs were 0.886 and 0.989 on day 14. All these ICC values are considered almost perfect according to the report of Landis and Koch.[29]

Imaging of CFP-Positive RGCs in Thy 1-CFP Mice by scSLO

For imaging individual RGCs, we performed scSLO of the retinas of Thy 1-CFP transgenic mice.[20] On the scSLO images, both brightly and weakly fluorescent cells of different sizes (Figs. 4A, left; 5A) were observed, a result consistent with the histologic findings of Raymond et al.[30] The CFP-positive cells were manually counted within four square areas at a distance of 830 μm from the center of the optic nerve head on the scSLO images (Fig. 5A, white squares). The distance of 830 μm was chosen as the shortest distance from the optic nerve head at which the CFP-positive cells could be accurately counted, without any influence of the retinal vessels. When an area closer to the optic nerve head is chosen, the large number of retinal vessels, which hide the CFP-positive cells from view, are included in the counting area. In addition, the density of RGCs and retinal nerve fiber bundles is higher as the area is close to the optic nerve head, which makes it difficult to precisely count the number of cells, particularly dark or small cells. The CFP-positive cells in GCL include displaced amacrines, and the displaced amacrines are small, with CFP fluorescence weaker than that of RGCs.[30] To exclude the displaced amacrines from the enumeration, we used the number of CFP-expressing cells, except for the weakly fluorescent small cells as the number of RGCs for the subsequent time-course and dose-dependence analyses of RGCs (see the Discussion section).

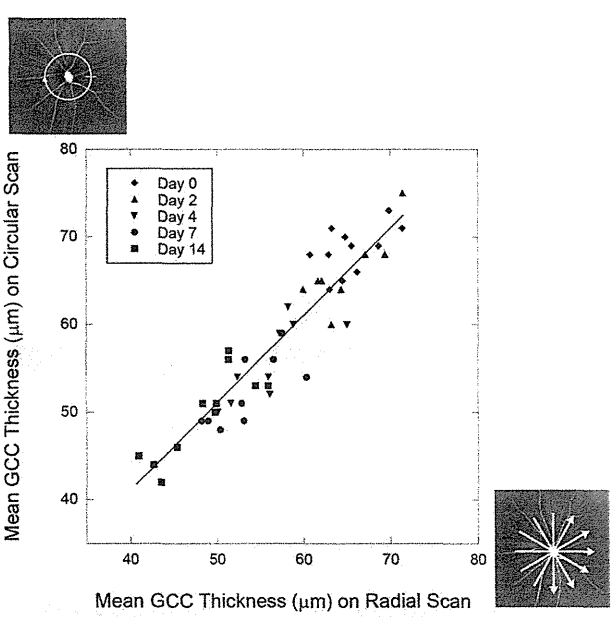

FIGURE 3. GCC thickness measured on a circular scan correlated well with the thickness measured on radial scans. GCC thickness measured on radial scans (x-axis) versus that on a circular scan (y-axis): r^2 = 0.908, $P < 0.001$, Pearson's correlation coefficient analysis.

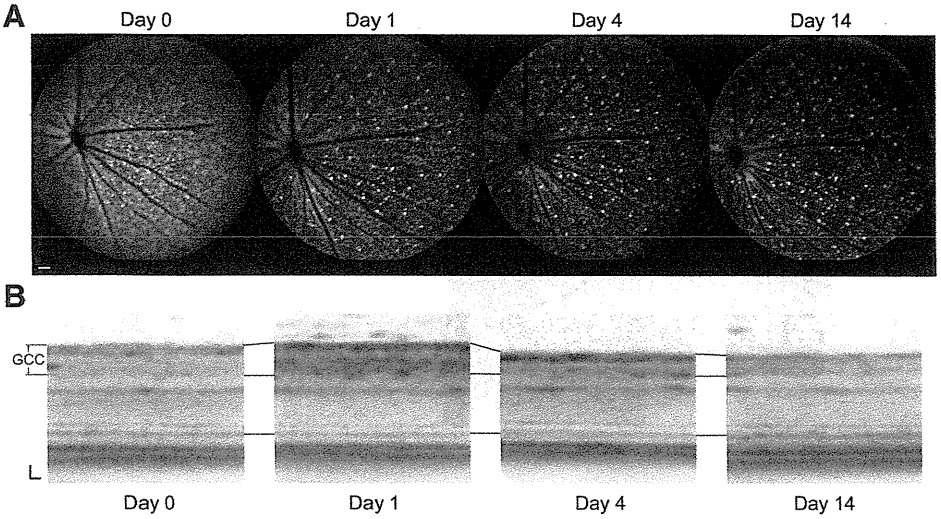

FIGURE 4. Simultaneous and longitudinal evaluation of the RGCs and the inner retinal layers after NMDA injection. (A) Images of Thy 1-CFP-positive RGCs using scSLO before (day 0) and after (days 1, 4, and 14) NMDA (20 nanomoles) injection. (B) Images acquired with speckle noise-reduced SD-OCT in the identical eye. Scale bar: (A) 100 μm; (B) 20 μm.

Time-Dependent Changes in the Number of RGCs and GCC Thickness in Identical Eyes after NMDA Injection

Next, we examined the time-dependent changes of the RGCs and the GCC thickness in the identical eyes after NMDA injection in Thy 1-CFP transgenic mice in detail. Simultaneous imaging by scSLO and SD-OCT was performed, and the number of RGCs (on scSLO) and the GCC thickness (on SD-OCT) were evaluated in the identical eyes at multiple time points. Figure 4 shows representative scSLO and SD-OCT images of a mouse eye before and after intravitreal injection of NMDA (20 nanomoles). Drastic reduction in the number of fluorescent spots was evident as early as 1 day after injection (day 1), compared with the number before injection (day 0), and then there seemed to be no change in the number of bright fluorescent spots from days 1 to 14 (Fig. 4A). Figure 5B shows the time-dependent changes in the number of CFP-expressing RGCs in mice injected with NMDA (20 nanomoles) and PBS. Although the number in the control eyes injected with PBS remained unchanged during the examination period, the mean number of RGCs in the eyes injected with NMDA dramatically decreased at day 1 (27.1% ± 7.6% [mean ± SD] of the preinjection level) and then slightly decreased from days 1 to 14 (Figs. 5B, 5D). After 14 days of NMDA injection, the number of CFP-positive RGCs decreased to 20.2% of the preinjection level. The number of RGCs in eyes injected with NMDA was significantly less than that in eyes injected with PBS after day 1 ($P < 0.0001$). To determine whether RGC loss followed a pattern at the early time points, we assessed the remaining CFP-positive RGCs in each quadrant on day 1 and found that the mean numbers were similar and did not show significant differences among the quadrants ($P = 0.886$, one-way ANOVA); the mean numbers were 19.1 ± 2.4, 17.3 ± 6.3, 17.8 ± 4.2, and 18.1 ± 5.7 (27.1%, 24.7%, 24.9%, and 26.3% of the preinjection level, respectively) in the superior, inferior, temporal, and nasal quadrants, respectively. Thus, the RGC loss on day 1 may be characterized by regional uniformity.

On the other hand, GCC thickness on the SD-OCT images did not appear to be thinned 1 day after NMDA injection and was apparently thinned from day 4 onward (Fig. 4B). In eyes injected with NMDA, the mean GCC thickness increased at day 1 ($P < 0.0001$, compared to day 0) and then started to decrease (Fig. 5C). After day 4, the GCC was significantly thinner than that before injection ($P < 0.0001$). There was a similar increase in GCC thickness in PBS control eyes at day 1 ($P = 0.01$). The GCC thickness decreased to preinjection levels at day 4 and remained unchanged thereafter through day 14 in the control eyes.

The relationship between the percentage reduction of the number of the RGCs and GCC thickness is shown in Figure 5D. One day after NMDA injection, the number of RGCs significantly decreased (to 27.1% ± 7.6%; mean ± SD). On the other hand, GCC thickness increased to 110.3% ± 6.1% on day 1. The RGCs only slightly decreased from days 1 to 14 (24.1% ± 4.5%, 22.7% ± 4.8%, 22.5% ± 4.3%, and 20.2% ± 5.1% compared to day 0, on days 2, 4, 7, and 14, respectively). In contrast, GCC thickness on day 2 was almost the same as that on day 0 (99.1% ± 6.5% of the preinjection level), then gradually decreased throughout the examination period (81.7% ± 4.3%, 75.6% ± 3.1%, and 71.4% ± 4.7% on days 4, 7, and 14, respectively). These results indicate that the decrease in the number of CFP-positive RGCs was followed by the thinning of the inner retinal layers.

Histologic Evaluation of the Effect of CFP Downregulation and Displaced Amacrines on scSLO Imaging after NMDA-Induced Injuries

There may be two problems in using Thy 1-CFP transgenic mice for monitoring RGCs: (1) the existence of displaced amacrine cells expressing CFP in GCL, as stated above and (2) CFP downregulation that occurs before RGC death. To study the response of the displaced amacrines to NMDA insult and the influence of these cells on our scSLO results, we performed immunohistochemical staining by using an anti-GFP antibody to detect CFP-positive cells and anti-HPC-1 to detect amacrines in the paraffin-embedded sections (Supplementary Fig. S1 and Supplementary Table S1, http://www.iovs.org/lookup/suppl/doi:10.1167/iovs.10-6654/-/DCSupplemental). The percentages of GFP-positive cells of all cells in the GCL were 83.0% at day 0 and 24.8% at day 14. The percentage of GFP-positive/CFP-negative (cells that possibly lost weak CFP fluorescence during sample preparation) of all GFP-positive cells was 2.6% at day 0 and 2.4% at day 14 in the frozen sections. These results suggest that GFP staining and fluorescence of CFP are almost identical and that the anti-GFP antibody is suitable for detection of CFP-positive cells (Supplementary Fig. S1A, http://www.iovs.org/lookup/suppl/doi:10.1167/iovs.10-6654/-/DCSupplemental). On day 0, the number of HPC-1-positive/GFP-positive cells in the GCL (displaced amacrines) was 20.0 ± 2.0 (6.5% of all the GFP-positive cells). After 14 days of NMDA injection, the number of HPC-1-positive/GFP-positive cells slightly decreased (15.7% ± 1.5%; 78.5% of the preinjection level, 34.6% of the remaining GFP-positive cells)

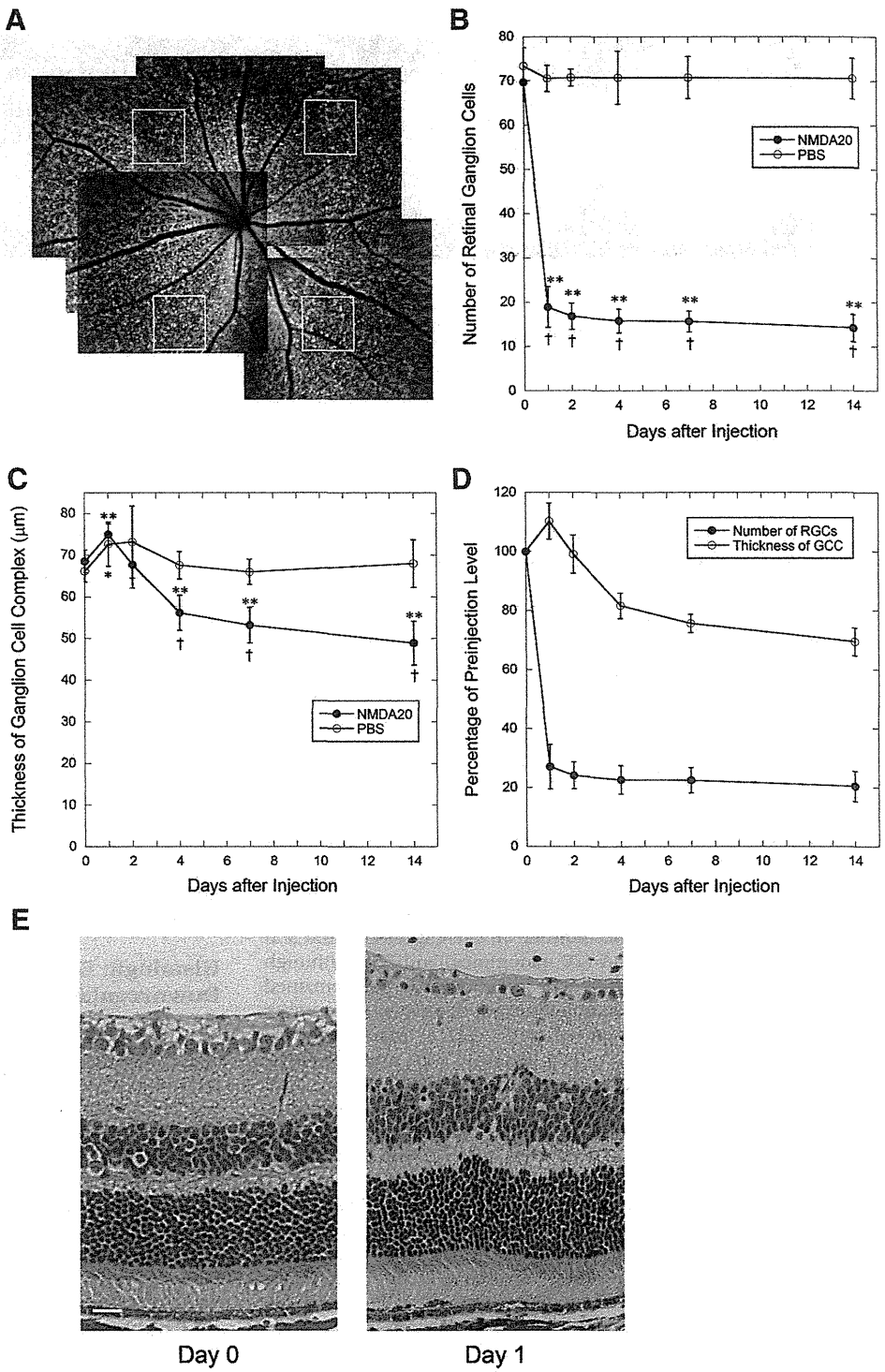

FIGURE 5. Time-dependent changes in the number of RGCs and the GCC thickness after NMDA injection. (**A**) A combined scSLO image of an untreated Thy 1-CFP mouse. The white squares (310-μm squares) indicate areas in which CFP-positive RGCs were counted. Longitudinal changes in the number of RGCs (**B**) and in GCC thickness (**C**) in mice injected with PBS and 20-nanomoles NMDA (for each, $n = 15$). (**D**) The percentage of RGCs and GCC thickness in the postoperative period versus that in the preoperative period. Error bars indicate SD. $^{*}P < 0.05$; $^{**}P < 0.0001$ compared with the preinjection level (paired *t*-test). $\dagger P < 0.0001$ compared between eyes injected with NMDA and PBS (*t*-test). (**E**) Images obtained on days 0 and 1 of retinal sections from eyes injected with NMDA (20 nanomoles) and stained with HE. The retina on day 1 appears to be thickened and particularly the IPL appears swollen. RGCs appear to be fewer on day 1, compared with day 0. Scale bar, 20 μm.

(Supplementary Fig. S1B, http://www.iovs.org/lookup/suppl/doi:10.1167/iovs.10-6654/-/DCSupplemental). Next, we focused on HPC-1-negative cells in the GCL, which could be considered to be mainly RGCs, to reveal the effect of CFP downregulation on the scSLO results. On day 1 after NMDA injection, HPC-1-negative cells decreased to 65.2% of the preinjection level. HPC-1-negative/GFP-positive cells decreased to 34.6% of the preinjection level. In contrast, HPC-1-negative/GFP-negative cells increased to 258.3% of the preinjection level. To confirm that the HPC-1-negative/GFP-negative cells contain RGCs, we performed triple immunostaining for HPC-1, Brn3 (an antibody for retinal ganglion cells[28]), and GFP (Supplementary Fig. 1C, http://www.iovs.org/lookup/suppl/doi:10.1167/iovs.10-6654/-/DCSupplemental). There were Brn3-positive cells that stained negative for HPC-1 and GFP cells, both before and after NMDA injection, suggesting that retinal ganglion cells are included in the HPC-1-negative/GFP-negative cell population. These results suggested that although CFP downregulation occurred in some cells, the number of RGCs indeed decreased as early as 1 day after NMDA injection. To further confirm that

RGC loss preceded reduction in GCC thickness, we compared the hematoxylin-eosin (HE)-stained retinal sections between days 0 and 1 (Fig. 5E). On day 1, the retina, particularly the IPL, appeared to be thickened. On the other hand, on day 1, the cells in the GCL decreased to 72.6% of that on day 0, as counted on the histologic sections. From these histologic observations, we confirmed that rapid loss of RGCs preceded the thinning of the inner retinal layers.

Dose- and Time-Dependent Changes in the Number of RGCs and GCC Thickness in Identical Eyes after NMDA Injection

To clarify the difference in the severity and time course of the damage caused by different dosage of NMDA, 1 to 20 nanomoles of NMDA (or PBS as a negative control) was injected in the eyes of Thy 1-CFP mice and examined with scSLO and SD-OCT. In eyes injected with 2 to 20 nanomoles of NMDA, the number of RGCs significantly decreased on day 1 and thereafter, whereas in the eyes injected with 1 nanomole of NMDA, RGCs only marginally decreased during the period, compared with eyes injected with PBS (Fig. 6A). Eyes injected with 10 or 20 nanomoles NMDA showed similar reductions in the number of RGCs on day 14 (28.3% and 20.2% of the preinjection level, respectively). However, the reduction was slower in eyes injected with 10 nanomoles of NMDA compared with those with 20 nanomoles of NMDA; the number of RGCs in eyes injected with 10 nanomoles of NMDA was larger than the number of RGCs in eyes injected with 20 nanomoles of NMDA on day 1 (49.5% and 27.1% of the preinjection level, respectively, $P = 0.002$ [Scheffé's test]), but was not significant on days 4 to 14. The eyes injected with 2 or 5 nanomoles of NMDA tended to show a smaller reduction in numbers compared with those injected with 10 or 20 nanomoles of NMDA throughout the postinjection period; the number of RGCs was 65.3% ($P = 0.003$) and 71.7% ($P = 0.004$) of the preinjection level, respectively, on day 1 and further decreased to 44.1% ($P < 0.0001$) and 53.7% ($P < 0.0001$) of the preinjection level, respectively, on day 14. Thus, NMDA dose dependently reduced the number of RGCs; a higher dose of NMDA induced more rapid and stronger loss of RGCs.

Consistent with the number of RGCs, 2- to 20-nanomole NMDA injections caused significant decreases in GCC thickness at day 4 and thereafter (Fig. 6B). As was the case with 20 nanomoles of NMDA injection (above), the GCC thickness did not significantly decrease until 4 days after the injection. PBS or a 1-nanomole NMDA injection did not decrease GCC thickness (Fig. 6B). In eyes injected with 5, 10, and 20 nanomoles of NMDA, GCC thickness decreased to 75.7%, 76.5%, and 71.4%, respectively, of the preinjection level on day 14; there were no statistically significant differences between the three groups (Scheffé's test). GCC thickness in eyes injected with 2 nanomoles of NMDA showed a lesser reduction (84.6% of the preinjection level) than those injected with 5 to 20 nanomoles ($P = 0.041$ vs. 5 nanomoles; $P = 0.021$ vs. 20 nanomoles) on day 14. These results show that decreases in the number of RGCs and in GCC thickness are NMDA dose dependent and that 2 nanomoles or more of NMDA is needed to induce a significant loss of RGCs and in GCC thickness.

Discussion

In this study, we used a novel, noninvasive imaging system combining scSLO and speckle noise-reduced SD-OCT to characterize the longitudinal and dose-dependent RGC degeneration induced by NMDA. Two nanomoles or more of NMDA induced rapid loss of CFP-expressing RGCs. The inner retinal layer became thin after the CFP-expressing RGCs disappeared. The NMDA-induced degeneration of RGCs and the inner retinal layers was dose-dependent.

The development of imaging instruments for clinical use provides a unique opportunity to apply these instruments to experimental animals for noninvasive, longitudinal assessment of progressive RGC damage. Recent studies have demonstrated that imaging of CFP-expressing RGCs in Thy 1-CFP transgenic mice using a blue-light confocal SLO or a fundus camera is useful for the longitudinal assessment of injuries to the bodies of RGCs in optic nerve crush and ischemia-reperfusion models.[7–9] Another study has shown that measuring RNFL thickness is also useful for longitudinally assessing axonal injuries of RGCs in an optic nerve crush model.[10] However, no studies have reported longitudinal assessments of RGC damage, both in the number of RGCs and in the thickness of the inner retinal layer by any method.

NMDA-induced excitotoxicity is a well-known model of induced RGC injury[23] and has been implicated in the pathogenesis of glaucoma. At first, we injected 20 nanomoles of NMDA into the vitreous of Thy 1-CFP mice and observed that the number of CFP-expressing RGCs decreased to less than 30% of the preinjection level as early as 1 day after injection and continued to decrease slightly from days 1 to 14 (Fig. 5). In contrast, GCC thickness increased at day 1 and then gradually decreased from days 2 to 14. This study clearly demonstrated that two distinct structural parameters (number of CFP-positive RGCs and GCC thickness), whose losses were recently established to represent RGC damage in vivo, behaved in a totally different manner during the time course of NMDA-induced RGC injury in a mouse model.

In rats, Nagata et al.[10] were not able to find RNFL thinning, even 1 week after optic nerve crush versus the 50% RGC loss that was reported in another study.[4] Although no study has directly compared the number of RGCs (based on Thy 1-CFP expression

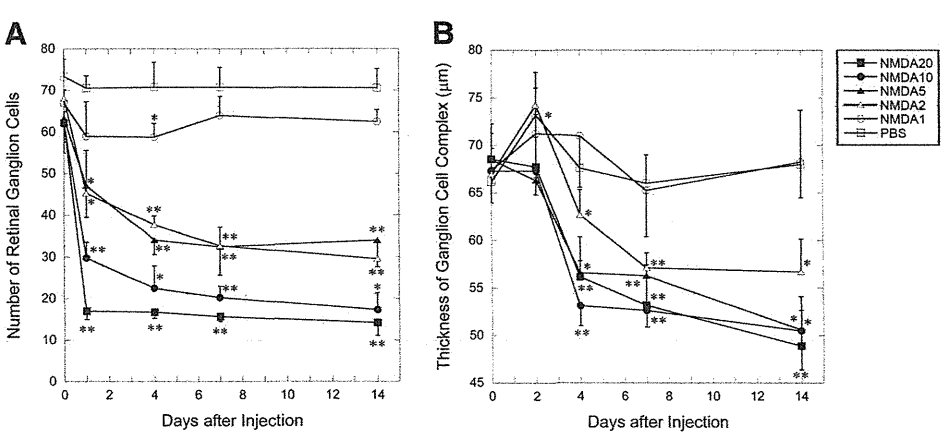

FIGURE 6. Dose- and time-dependent changes in the number of RGCs and in GCC thickness in identical eyes after NMDA injection. Longitudinal changes in the number of RGCs (A) and in GCC thickness (B) in mice injected with PBS ($n = 15$) and NMDA (1, 2, 5, 10, and 20 nanomoles; $n = 6$, $n = 10$, $n = 10$, $n = 15$, and $n = 15$, respectively). $^*P < 0.05$; $^{**}P < 0.0001$ compared to the preinjection level (paired t-test).